PCCP

Accepted Manuscript

ROYAL SOCIETY OF CHEMISTRY

www.rsc.org/pccp

Journal Name

ARTICLE

Enhanced Photophysical properties of plasmonic-magnetic metal-alloyed semiconductor heterostructure nanocrystals : A case study for Ag@Ni/$Zn_{1-x}Mg_xO$ system

Received 00th January 20xx,
Accepted 00th January 20xx

DOI: 10.1039/x0xx00000x

www.rsc.org/

Sumana Paul, Sirshendu Ghosh*, Manas Saha and S. K. De*

Understanding the effect of homovalent cation alloying in wide band gap ZnO and formation of metal-semiconductor heterostructure is very important for maximisation of photophysical properties of ZnO. Nearly monodispersed ZnO nanopyramid and Mg alloyed ZnO nanostructures have been successfully synthesized by one pot decomposition of metal stearate by using oleylamine both as activating and capping agent. The solid solubility of Mg(II) ions in ZnO is limited to ~30% without phase segregation. An interesting morphology change is found on increasing Mg alloying: from nanopyramid to self assembled nanoflower. The morphology change has been explained by oriented attachment process. Introduction of Mg in ZnO matrix increases the band gap of materials and also generates new zinc interstitial (Zn_i) and oxygen vacancy related defects. A plasmonic magnetic Ag@Ni core shell (Ag as core and Ni as shell) nanocrystals has been used as a seed material to synthesize Ag@Ni/$Zn_{1-x}Mg_xO$ complex heterostructures. An epitaxial growth has been established between Ag(111) and ZnO(110) planes in the heterostructure. An epitaxial metal semiconductor interface is very crucial for complete electron-hole (e-h) separation and enhancement of the exciton life time. The alloyed semiconductor-metal heterostructure has been observed to be highly photocatalytic active for dye degradation as well as photodetection. Incorporation of magnetic Ni(0) makes the photocatalyst superparamagnetic at room temperature which is found to be helpfull for catalyst regain.

Introduction:

Nanoscale heterostructured materials are currently of great interest from the application point of view in the field of interdisciplinary nanoscience. Among the various kinds of heterointerface, semiconductor-semiconductor, metal-semiconductor and core-shell heterostructure are found to be very important to engineer physiochemical properties[1]. Metal-semiconductor heterostructures are the most intriguing one for their multimodal applications in wide field like sensing[2], magnetic, catalysis[3], biology[4], photovoltaics[5], photocatalysis[6] and more. In metal-semiconductor heterostructure, a coupling between the quantum confined excitonic states of semiconductor and dielectrically confined electronic states in the metal part is expected for efficient interaction between metal and semiconductor. In particular, noble metal-semiconductor hybrid structured NCs have become a most attractive topic in research due to tunability of optical properties in a wide spectral range. The excitation of localized surface plasmon resonance (LSPR) of metal nanocrystals (NCs) often enhances the photophysical properties of closely situated semiconductor NCs and even generates new functionality. Au, Cu and Ag metal NCs are found to be highly efficient light absorber in UV-Vis and also NIR region depending upon size, shape and degree of alloying for their strong and stable LSPR phenomenon. For example improved photocatalytic properties have been reported in Au-ZnO[7], Au-CdSe[8], Au-TiO_2[9] , Au-SnS[10] and Au-Cu_2ZnSnS_4 [11] hybrid nanostructures.

The wide band gap metal oxides such as TiO_2 and ZnO are the most attractive class of semiconductor because these materials have high catalytic efficiency, low cost and are environmentally sustainable. ZnO is a common and inexpensive green material with high electron mobility and large carrier concentration due to intrinsic defects and proved to be a promising candidate as transparent conducting oxide (TCO) coatings[12,13], photocatalyst[14], gas sensors[15], photodetector[16]. The combination of plasmonic metal NCs (Au, Ag, Cu) with the ZnO nanostructure improves the photocatalytic[7] and gas sensing performances[17] of ZnO. To maximize the photocatalytic process of semiconductor, it is important to achieve the photo-induced charge separation by the band gap excitation of the semiconductors. Also the increase in exciton lifetime enhances the photoresponse property of material. Fast recombination of electron-hole pairs is undesirable and always leads to a reduced photocatalytic efficiency and poor photoresponse. One of the promising ways to prevent the fast recombination of photogenerated electron and hole is to combine the ZnO with metal NCs to form a hybrid heterostructure. Metal NCs can act as an electron sink (for high electron affinity and lower

Department of Materials Science, Indian Association for the Cultivation of Science, Kolkata-700032, India. Email: mssg2@iacs.res.in, msskd@iacs.res.in.
Electronic Supplementary Information (ESI) available: See DOI: 10.1039/x0xx00000x

Fermi energy level) which can accept the photogenerated electrons from semiconductor and increase the exciton lifetime. Efficient electron transfer is only possible if the metal and semiconductor moieties are connected by the epitaxial crystallographic relation. Direct contact of metal through epitaxy can lead to effective charge separation and enhance interfacial charge-transfer which can promote photocatalytic efficiencies and photoresponse.

Photochemically charged ZnO colloidal NCs were established as a powerful reductants[18-20]. Detailed experimental studies prove that Mg^{2+} alloying in ZnO not only widen the band gap but also increase the conduction band potential and lower the valence band potential in a ratio of ΔE_{CB}: ΔE_{VB} = 0.68:0.32 which makes Mg alloyed ZnO more reducing than pure ZnO[21]. Theoretical calculation also predicts more reducing capability of Mg alloyed ZnO than the pure one[22,23]. So from literature survey, we find two ways to make ZnO more photocatalytic, either by making proper epitaxy between metal and semiconductor or Mg alloying in ZnO. Almost similar tetrahedral ionic radius of Mg^{2+} (0.57 Å) and Zn^{2+} (0.60 Å) gives rise to high solid solubility of Mg^{2+} in wurtzite ZnO[24]. $Zn_{1-x}Mg_xO$ thin films have been prepared by different solid state techniques like pulsed laser deposition (PLD)[25], molecular beam epitaxy[26], magnetron sputtering, chemical vapor deposition[27] and chemical method like sol-gel deposition. Synthesis of colloidal $Zn_{1-x}Mg_xO$ NCs with well defined shape is very limited[28,29].

Here we report the synthesis of nearly monodispersed ZnO and $Zn_{1-x}Mg_xO$ NCs by thermal decomposition process via a one pot reaction taking metal-stearate compound as the metal ion source and oleylamine as the activating and capping agent. The Mg^{2+} ion incorporation into wurtzite matrix has an unusual effect on shape evolution of the $Zn_{1-x}Mg_xO$ NCs. On Mg^{2+} alloying, the perfect pyramidal structure of pure ZnO changes to flower like morphology. The present observation is quite different from previously reported $Zn_{1-x}Mg_xO$ system where Mg^{2+} incorporation changes the shape from small nanopyramid to nanorod for the preferential growth of material along the c-axis[28,29].

A series of Au-ZnO hybrid nanostructures including pyramid[30], nanorods[7], nanourchin[31] shaped of ZnO NCs have been studied. Some reported methods show uncontrolled deposition of Au on ZnO without any proper epitaxy. Excellent epitaxial interface between Au and ZnO and enhanced photocatalytic activity have been reported by Tahir et. al[7]. As the Au is a precious metal, large scale commercial applications of such nanoheterostructures (NHS) would be limited. Here we use Ag for the fabrication of metal-alloyed semiconductor heterostructure for two reasons: (i) more cost-effective and (ii) the Fermi level position of Ag metal (- 4.7 eV) is higher than that of Au (- 5.1 eV)[32]. The appearance of Fermi level of Ag closer to conduction band edge of ZnO makes energetically more favorable for transfer of photoexcited electron from ZnO to Ag metal. However, the density of states of unoccupied energy levels in the metal at the conduction band edge of a semiconductor determines the rate of electron transfer between photoexcited semiconductor and metal. Besides, the ZnO NCs contain a large amount of defect states in the band gap region (regardless of synthesis procedure). So one might prefer a metal whose Fermi energy level lies in the close vicinity of CB edge to quench the radiative transitions to defect states and consequently to gain higher photo efficiency.

Due to the high cost of the noble metals like Ag or Au large scale commercial application of these metal-semiconductor NHS would be restricted. One of the solutions lies in the fact by isolating the catalyst through physical method after each cycle of catalysis and reusing it. The easiest way is the introduction of magnetic property in the heterostructure so it can be magnetically separable. From literature study[33,34] we found that Ag@Ni and Ag@Pd core shell structures exhibit room temperature ferromagnetism and can be separable by small magnet from solution. We have chosen Ag@Ni core-shell structure (the lower cost of Ni) to form photo-catalyst metal-semiconductor NHS for the easy physical separation of the catalyst after each cycle of catalysis making the overall process a cost effective one.

Here we report an easy one pot green synthesis procedure of $Ag@Ni/Zn_{1-x}Mg_xO$ ternary NHS. The synthesis procedure involves first synthesis of Ag@Ni core shell as seed material from non-toxic silver and nickel salt and in-situ growth of $Zn_{1-x}Mg_xO$ NCs over metal NCs. Both for the pure and alloyed systems are found to be epitaxially related to Ag (111) plane of Ag@Ni moiety. An interesting shape change occurs for heterostructure and pure alloyed system on Mg^{2+} alloying. Here we investigate both the effects of Mg alloying and plasmonic magnetic metal-semiconductor formation on photophysical properties of ZnO.

Experimental section:

Materials: Zinc stearate ($Zn(st)_2$), magnesium stearate ($Mg(st)_2$), trioctylphosphine (TOP) and 1-octadecene [ODE, 90%] were purchased from Alfa Aesar. Oleylamine [(OLAM), 70%, tech], nickel acetylacetonate [$Ni(acac)_2$] and tetrachloroethelene (TCE) were purchased from Aldrich. N-butylamine (GR), acetonitrile (GR), n-octane (GR), silver nitrate (GR), ethyl alcohol (GR), acetone (GR), n-hexane (GR) and toluene (GR) were purchased from MERCK. All chemicals were used as received without any purification.

Synthesis:

Synthesis of ZnO and Mg doped ZnO ($Zn_{1-x}Mg_xO$) NCs:

Pure ZnO and $Zn_{1-x}Mg_xO$ NCs were synthesized with varying 'x' as 0.05, 0.10, 0.20, 0.30, 0.40 and 0.50. In order to prepare ZnO NCs 1 mmol of $Zn(st)_2$ was mixed with 5 ml of ODE in a 25 ml round bottom three neck flask fitted with a reflux condenser. Initially the mixture was evacuated for 30 min at room temperature. Then temperature was gradually increased to 90°C under constant evacuated condition. N_2 gas was purged into the three neck flask and 5 ml of degassed OLAM at 120°C was injected into that solution and was kept for 1 hr. The solution was turned into transparent yellow color. The transparent solution was again heated to 280°C and reaction was continued for 60 min. After completion of reaction, the

solution was cooled down to room temperature and 5 ml of n-hexane was added to this solution. The product was obtained by precipitation of the solution by adding excess ethanol as a polar solvent. The product was collected by centrifugation at 10,000 rpm for 3 min. The centrifugation was repeated for 3 to 4 times to remove impurities. The NCs were well soluble in non polar solvents like hexane, toluene, TCE etc.

The $Zn_{1-x}Mg_xO$ NCs were prepared under the same reaction condition by adding $Mg(st)_2$ in the required stoichiometric amount in ODE.

Synthesis of Ag@Ni nanoparticles:

Ag@Ni core shell nanoparticles were synthesized by one-pot seed growth method. Here $Ni(acac)_2$ and $AgNO_3$ were thermally decomposed in oleylamine. First of all $Ni(acac)_2$ and $AgNO_3$ were mixed with 6 ml of OLAM in 4:1 ratio in a three neck round bottom flask. Then 0.05 ml of trioctylphosphine (TOP) was added to it. The mixture was kept at vacuum for 20 min and the temperature was increased to 80˚C. The reaction was continued for 15 min under this condition and after that N_2 gas was purged into the solution. Then the reaction temperature was increased to 170˚C slowly and reaction was continued for 60 min. After completion of reaction, the solution was cooled down to room temperature, hexane was added to the reaction solution and product was collected by centrifugation of the solution by adding excess ethanol as a polar solvent. The centrifugation was done at 10,000 rpm for 3 min.

Preparation of Ag@Ni/$Zn_{1-x}Mg_xO$ NHSs:

Metal-semiconductor NHSs can be synthesized by two procedures. First by growing metal core and followed by deposition of semiconductor on it and second is vice-versa. We followed the first procedure to prepare $Ag@Ni/Zn_{1-x}Mg_xO$ NHSs. $Ni(acac)_2$ and $AgNO_3$ in 4:1 molar ratio were taken in 6 ml OLAM and 0.05 ml TOP in a three neck flask. After the complete formation of Ag@Ni at 170˚C reaction system was cooled down. At 80˚C temperature under N_2 gas atmosphere, $Zn(st)_2$ and $Mg(st)_2$ in the required stoichiometry were added to the solution and reaction was conducted at 280˚C for 1 hr. The washing procedure is same as pure system.

Characterization:

The crystalline phases of the products were determined by X-ray powder diffraction (XRD) by using Bruker AXS D8SWAX diffractometer, with Cu Kα radiation (λ = 1.54 Å), employing a scanning rate of 0.5˚ S^{-1} in the 2θ range from 20˚-80˚. For XRD measurement the TCE solution of the NCs was drop cast over amorphous silicon sample holder till a necked eye visible thin layer was formed. Transmission electron microscopy (TEM) images, high angle annular dark field scanning TEM (HAADF-STEM) images and energy dispersive spectrum (EDS) were taken using an Ultra high resolution field emission gun transmission electron microscope (UHR-FEG TEM, JEM-2100F, Jeol, Japan) operating at 200 KV. For the TEM observations, the sample was dissolved in TCE and was drop casted on a carbon coated copper grid. The room temperature optical absorbance of the samples was measured by a Varian Cary 5000 UV-VIS-NIR Spectrometer. Room temperature photoluminescence (PL) measurements were carried out with a Fluorescence Spectrometer (Hitachi, F-2500). Nitrogen sorption isotherms were obtained using a Quantachrome Autosorb 1C surface area analyzer at 77 K.

Thin film preparation and measurements:

Long chain OLAM was first replaced by n-butylamine by standard ligand exchange procedure. The n-butylamine capped nanomaterials were found to be well soluble in octane. A 2×2 mm^2 ITO substrate was first etched in the middle by using zinc dust and 1N HCl solution. Tthe substrate was further cleaned with de-ionised (DI) water and ethanol thoroughly and dried at 120˚C in N_2 atmosphere for 4 hr. Then total 0.2 ml of NHS/NC solution in octane (30 mg ml^{-1}) was spin casted on clean etched area of ITO substrate at a speed of 1000 rpm for 60 sec and dried it for 15 min in air. After each spin coating ITO part was cleaned with octane. The film was annealed in Ar atmosphere for 3 hr at 250˚C. Electrical contact was made by Ag paste with ITO parts. Photoresponse of the sample was measured using Keithley Electrometer 6517A and Keithley multimeter 2000 using computerized program.

Photocatalytic activity study:

Photocatalytic activities of Mg doped ZnO and $Ag@Ni/Zn_{1-x}Mg_xO$ samples were analyzed through Rhodamine B dye degradation technique in presence of light source KRATOS, Analytical instruments, universal Arc lamp supply-250 watt, 150XE, model no 1152. Rhodamine B (RhB) and the catalysts (0.02 gm, n-butylamine capped ZnO and $Ag@Ni/Z_{1-x}Mg_xO$ NCs calcined at 250˚C) were added to a 100 ml beaker containing 67 ml of de-ionized water. After ultra sonication, RhB dye (0.5 ml, 1 mmol/L) was injected to the above solution and was stirred for 2 hr in dark. Photocatalytic test was conducted and 3 ml of sample at different reaction time was centrifuged for the absorbance measurement using Varian Cary 5000 UV-VIS-NIR spectrophotometer.

Results and discussion:

Fig. 1 shows the XRD pattern of the pure ZnO and $Zn_{1-x}Mg_xO$ NCs where x varies from 0.05 to 0.5. The characteristic peaks are found to be well matched with hexagonal wurzite structure of ZnO (JCPDS no-36-1451, space group $P6_{3mc}$.) No impurity phase regarding the formation of MgO phase was observed up to 30% doping. At higher doping concentration (40%), a peak indexed (200) associated with cubic MgO appears. The smaller ionic radius of Mg^{2+} (0.057 nm) compared to Zn^{2+} (0.06 nm) generates lattice strain in $Zn_{1-x}Mg_xO$ alloy system. Size (D) and lattice strain (η) influence the shape parameters of XRD peaks

and can be simultaneously evaluated by following Williamson–Hall equation[35,36]:

$$\frac{\beta cos\theta}{\lambda} = \frac{1}{D} + \eta \frac{sin\theta}{\lambda} \qquad (1)$$

We have plotted $\frac{\beta\cos\theta}{\lambda}$ against $\frac{\sin\theta}{\lambda}$ to get crystal strain from the slope and particle size from intercept of straight line. Table S1 also shows the values of particle size and crystal strain of the NCs. Two types of strain can be generated in a doped crystal viz: tensile strain and compressive strain depending on the relative ionic radius of host and dopant ions. ZnO and $Zn_{1-x}Mg_xO$ samples reveal compressive strain as summarized in Table S1. This suggests that the strain plays an important role during the growth process.

XRD pattern of the as prepared Ag@Ni core shell nanoparticles are shown in the Fig. S1a. The diffraction peaks are assigned to the fcc Ag and Ni. Fig. S2 shows XRD peaks of the $Ag@Ni/Zn_{1-x}Mg_xO$ heterostructures. The XRD pattern reveals three crystalline phases of the samples which are fcc Ag, fcc Ni, and hexagonal wurzite ZnO. The heterostructure formation does not affect the solubility of Mg doping in ZnO lattice.

TEM analysis:

Fig. 2a shows the large area TEM image of nearly monodispersed ZnO NCs with very low degree of agglomeration. The inset shows a tilted view of single NC which depicts pyramid shape of the particle. The average dimension of the pyramid is found to be 30 ± 5 nm along the height with basal length nearly 37 ± 5 nm. Fig. 2b shows the HRTEM image of a single nanopyramid along the tip direction i.e. c-axis. The inner part shows higher contrast than the outer region of the pyramid. The image shows a perfect hexagonal base of the pyramid. The corresponding FFT pattern in Fig. 2c indicates that the NCs are single crystalline. The assigned planes from FFT pattern are (100), (010), $(1\bar{1}0)$ and (110). The nanopyramid grows along the (110) direction (with d = 0.16 nm). The surface is found to be terminated by the (100) group of (d = 0.28 nm) planes which are parallel to basal edges. The side surfaces of nanopyramids consist of polar {101} facets which are the most exposed surfaces in the NCs. Oleylamine which was used as activating and capping agent in our synthesis protocol has a strong effect on stabilizing the polar facets like {001}, {101} etc. The polar head -NH_2 of oleylamine molecule can bind to the thermodynamically unstable Zn-rich facets and can stabilize a near perfect pyramid shape.

Fig. 2d and 2g show large area TEM images of 10% and 20% Mg alloyed assembled ZnO NCs. Although a morphological change has been observed but the colloidal stability and well dispersion nature of the product remains unaltered. The general image and the tilted view at inset in Fig. 2d predicts that the NCs are formed by in-situ self assembly but maintained the hexagonal base nature. The morphology of 20% Mg doped ZnO NCs is flower like shape without perfect hexagonal base. Normally homovalent dopant like Cd^{2+} or Mg^{2+} changes the morphology from pyramid to nanowire/nanorod by accelerating the growth along c-axis of ZnO[28,29]. The present observation of self assembly of NCs is quite different from the previous results. The degree of self assembly increases with Mg concentration. The HRTEM and the corresponding FFT patterns in Fig 2e and 2f show a single crystalline nature of the NCs although a large amount of void spaces exists in the nanoflower. Here we believe that oriented attachment (OA) process drives the formation of self assemble structure. The OA process in colloidal synthesis generally occurs in presence of inorganic anion which can be absorbed onto a particular facet of NC. Consequently it decreases solubility of NCs and accelerates the OA of facets.[37] Such possibility can be ruled out in our synthesis protocol as the reaction mixture does not contain any inorganic anion since both the Zn and Mg sources were supplied from stearate salts. The dopant ions can generate or increase the surface charge/local dipole moment by introducing the surface defect states (*vide infra* in PL section) and increase the chemical attraction forces between the NCs. This favors the attachment of similar crystallographic planes or facets of two or more NCs and leads to nearly self-assembled single NC with higher volume through OA process. The size of the assembled alloyed NCs (10% Mg doped ~ 45 nm, 20% Mg doped ~ 60 nm) are found to be higher than the pure one. The Mg alloyed ZnO nanoflowers can be considered as the self assembly of some small sized nano 'petals' which are formed at the early stage of growth process and undergo coalescence on the latter stage to generate nearly single crystalline nanoflower. Homovalent (Co^{2+}, Mn^{2+}) or aliovalent ion (In^{3+}, Ga^{3+}) doping in ZnO NCs decreases the crystallite size.[12,38] The decrease of crystallite size upon doping can be explained by the Gibbs–Thomson relationship.[38]

$$S_r = S_B \exp[\frac{2\sigma V_m}{rRT}] \qquad (2)$$

Where S_r is the solubility of the crystallite of radius r, S_B is the solubility of the corresponding bulk material, V_m is the molar volume, and σ is the specific surface energy of NCs. The dopant resides at surface or near surface causes lattice strain (also observed from XRD analysis) that elevates the specific surface energies, σ, and increases the crystallite solubility. So initially, the Mg alloying decreases the crystallite size of ZnO and decreased crystallites undergo coalescence to give self assembled morphology/nanoflower.

As there was no change in surface protecting ligand on Mg-alloying, we can speculate Mg alloying not only decreases the particle size but also introduces some defects (missing of one or few atoms or interstitial ions) in non-polar facets of wurtzite ZnO (which will be discussed in PL section). Such defects can generate local dipole moment at the facet and can accelerate the coalescence along that facet. Although most of the particles in 10% Mg alloyed ZnO were found to be single crystalline but for 20% Mg doped ZnO NCs presence of twin

plane is very often. The imperfect OA leads to the formation of twin boundaries. A representative HRTEM image has been shown in Fig. 2h. The FFT pattern of the image (Fig. 2i) shows the twin planes of (010), (020) and $(1\bar{1}0)$. The perpendicular facets of (010) direction are {001} and {002}. The würtzite ZnO crystal consists of alternating planes composed of fourfold tetrahedrally coordinated Zn^{2+} and O^{2-} ions, staked alternatively along the *c*-axis. So the Zn^{2+} rich positively charged {001}/{002} facets of one NCs and O^{2-} rich negatively charged {001}/{002} polar facets of other one might come closer to undergo OA during the growth process. Figure S3 in ESI shows an atomic model of OA along (010) direction. Also the {010} and {110} facets are involved for OA along $(1\bar{1}0)$ direction. Although the {010} and {110} facets are neutral (ESI, Fig. S4) but incorporation of Mg^{2+} ions in interstitial lattice position might create local charges which accelerates the OA process along $[1\bar{1}0]$ direction.

Fig. S5, S6 and S7 in ESI show TEM images early from reaction time to understand OA growth of 20% Mg doped ZnO NCs. TEM images in Fig. S5 of reaction product collected at 15 sec indicate the lowest size (20 – 30 nm) assembly of nanoparticles. Each assembly consists of 4 - 5 nanocrstals with size range of 5-10 nm. Fig. S5b shows the grain boundary region. The appearance of twin (010), $(\bar{1}00)$ and $(1\bar{1}0)$ planes in FFT (Fig. S5) of yellow square region suggests OA process. So Mg dopnats reduce the crystallite size and induce OA process. Fig. S6 shows the TEM image after 1 min of reaction. Marked area in Fig S6a shows assembly of small assembles. Closer look in Fig S6b shows nearly 6-7 small assembly (20 - 25 nm in size) further undergo coalescence to form larger size cluster. FFT from different grain boundary area shows that OA process is operating along [011] and [010] direction. Fig.S7 shows TEM images of 10 min reaction product. Most of the self-assembled clusters are in 35 - 50 nm size (Fig. S7b). Twin structures in FFT (Fig. S7c) indicate a clear evidence of OA process.

30% Mg alloyed ZnO samples show a decrease in size of nanoflower as evidenced from Fig. 2j. The nanoflower assembly only contains 3-4 petal units nearly ~ 15 nm of size (Fig. 2k). HRTEM in Fig. 2l shows a single petal with growth along (002) direction. The HRTEM image also shows the presence of amorphous layer probably coming from surface segregation of MgO moiety which impedes the OA process resulting a decrease in nanoflower size. 40% Mg doped ZnO sample does not show any self assembly or oriented attachment (Fig. 2m). A high decrease in nanopyramid height (thickness ~ 5- 7 nm) is found from HRTEM images in Fig. 2n. The corresponding FFT pattern in Fig. 2o shows the presence of (110) plane. So on Mg alloying the crystallite size of ZnO NCs decreases on increasing Mg%. The reduced size $Zn_{1-x}Mg_xO$ NCs participates in oriented attachment to yield a free standing flower like morphology and degree of OA is maximum at 20% Mg alloyed system. For higher alloying % the OA process is quenched for amorphous layer formation around each NC. Actual alloy percentage of Mg in ZnO has been estimated by EDS analysis and has been given in Fig. S8 in ESI. Fig. S9 and S10 shows the element mapping and EDS line scan of 20% Mg alloyed ZnO sample which shows a homogenous distribution of Mg in ZnO system.

Figure S11a [ESI] shows representative TEM image of as-synthesized Ag@Ni core-shell structure. The NCs have usually spherical morphology or prolate type. HRTEM image in Fig S11b indicates that the particle has two distinct regions: a darker core region with a lighter shell. The higher Z value of Ag at core has higher electron scattering ability than the lighter element Ni at shell region. The shell thickness varies as 1.5 – 2.5 nm. Fig. S11c shows the FFT pattern of the interfacial region of Ag and Ni phases as highlighted by the squared area in Fig. S11b. The reconstructed HRTEM image by masking the yellow circled spots shows the (200) plane of Ag (d = 0.208 nm) (Fig. S11d), whereas the white circled spots show the (210) plane of Ni (d = 0.178 nm) (Fig. S11e). Some dislocations are observed in reconstructed HRTEM images. This dislocation may be formed for the lattice deformation at core-shell interfacial region which often observed in quasi-epitaxial growth of core shell or heterostructure[39,40]. Selected area diffraction (SAED) pattern obtained from these nanoparticles (Fig. S11f) shows diffraction rings that are mainly composed of face-centered cubic (fcc) Ag and Ni.

Fig. 3a shows the large area TEM image of as-synthesized Ag@Ni/ZnO NHSs. The image depicts that ZnO nanopyramids are connected with one or more spherical shape and darker in contrast Ag@Ni metal moieties. Interestingly the morphology of ZnO does not change in presence of Ag@Ni seeds during the synthesis. Fig. 3b shows the HRTEM image of a single heterostructure at the site of interest where the interface between metal and semiconductor is believed to be formed. Metal area shows a distinct core shell nature with darker core as Ag and lighter shell Ni. Form literature[7] study in Au/ZnO heterostructure, we can generalize in most of the cases metal NC (Au) always preferred to situate at the tip or base of ZnO pyramid with a growth of ZnO along (001) direction over Au(111) planes. In the present case, Ag NCs are randomly situated at tip and facets of ZnO pyramid. Fig. 3c shows the FFT pattern obtained from the yellow squared area of Fig. 3b, i.e. the pure ZnO region. The reconstructed HRTEM image (Fig. 3d) shows the presence of (102) and (110) planes of ZnO. Fig. 3e shows the FFT pattern obtained from the orange squared area of Fig. 3b. The FFT contained large number of spots which are the reflection of planes both from Ag@Ni and ZnO part as the FFT was taken at interface region. We can establish an epitaxial growth of ZnO onto Ag from FFT. The calculated d value from white circled spots is 0.235 nm which is the reflection of Ag(111) plane. Another one set of spots are found at nearly same direction (cyan colour spots). The plane from this spot is found to be (110) of ZnO with d-spacing value 0.161 nm. The simulated HRTEM image by masking these two

colored spots are presented in Fig. 3f, which shows a co-inside of Ag(111) plane and ZnO(110) plane. We can generalize the epitaxial relation by the periodic arrangement of 2Ag (111) planes (2×0.235 nm = 0.47 nm) with 3ZnO (110) planes (3×0.16 nm = 0.48 nm). The co-incidence of 2d (111) of Ag with 3d (110) of ZnO is highlighted by marking straight line for visibility in Fig. 3f. Atomic arrangement of (111) planes of Ag and (110) of ZnO and matching between 2d (111) with 3d (110) planes has been shown in ESI Fig. S12.

Fig. 4a shows a typical large area TEM image of $Ag@Ni/Zn_{0.8}Mg_{0.2}O$ metal alloyed semiconductor NHS. A striking morphological change of semiconductor part is found similar to non-metal decorated system. Inverted bright field TEM image (Fig. 4b) shows flower like morphology decorated with spherical metal NCs. Higher magnification view depicted in Fig. 4c shows each nanoflower is connected with multiple metal NCs. Such hybrid heterostructures are colloidally stable in ambient condition over the months. Fig. 4d shows a typical HRTEM image of site of heterostructured nanoflower where both the Ag and alloyed ZnO are present. The image clearly depicts the Ag NC is attached to three nanopetals. To verify the epitaxy formation the FFT pattern from the interface region is depicted in Fig. 4e. The (111) plane for Ag corresponding to d value (d_1 = 0.23 nm) has been identified and marked as white circle. Along the same direction of Ag(111) plane we also identified (012) plane of ZnO with d-spacing value of 0.191 (d_2) nm highlighted in cyan circle. The simulated HRTEM image in Fig. 4f by masking these two set of spots shows the interface region of Ag and ZnO. The lattice mismatch between Ag(111) and ZnO(012) planes was calculated using the following formula:

$$\eta = \frac{|d_1 - d_2|}{0.5(d_1 + d_2)} \times 100\% \qquad (4)$$

The value of η is found to be ~ 18% based on the estimated d values from HRTEM image. The prediction of epitaxial growth is consistent with earlier reports for a wide lattice mismatches between metal and semiconductor.[41]

The FFT pattern obtained from the yellow square area (pure alloyed ZnO region) in Fig. 4d is presented in Fig. 4g. We have identified mainly (020) and (012) planes of ZnO viewed along a-axis. A closer view of (012) spots shows that each spot is the overlap of two distinct spots highlighted in yellow circle. The reconstructed HRTEM image from the FFT (in Fig. 4h) shows the presence of twin (012) plane of ZnO and (020) plane. The yellow square area in Fig 4d which is the joining region of two ZnO petal is mainly single crystalline in nature (as observed from reconstructed HRTEM image in Fig. 4h) and the two petals are attached by the twin (012) plane of ZnO. The reconstructed HRTEM image also shows a considerable amount of dislocation (black arrows) at the joining region. Such kind of defect is normally observed for imperfect OA involving multiple smaller size NCs. To further understand the growth process of this metal alloyed semiconductor heterostructure we quenched the reaction at 10 min and carried out TEM analysis for intermediate product. Fig. S13 in ESI shows the TEM image of $Ag@Ni/Zn_{0.8}Mg_{0.2}O$ sample collected at 10 min of reaction. The image indicates mainly metal (Ag)-semiconductor (ZnO) dimer where the ZnO part has 10-15 nm in size (much smaller than the final nanoflower dimension). The entire metal domain is situated with smaller ZnO nanoparticle. The image also shows the presence of some free standing ZnO (not connected with metal domain). So this free standing ZnO NCs and Ag-ZnO dimer might undergo OA with each other or with self-type and gives the beautifully grown metal decorated alloyed nanoflower on complete reaction of 60 min. The metal domain size remains unaltered and does not undergo coalescence (metal-metal attachment). The coalescence occurs between $Ag@Ni/Zn_{1-x}Mg_xO$ and pure $Zn_{1-x}Mg_xO$, one $Ag@Ni/Zn_{1-x}Mg_xO$ with other metal decorated $Zn_{1-x}Mg_xO$. The final product appears to be a nanoflower decorated with multiple metal domain accompanied with multiple crystal plane dislocation.

Optical property study:

The effective band gap was investigated from UV-VIS absorption spectra of the as prepared samples at room temperature (Fig. 5a). An abrupt absorption edge is observed at about 362 nm corresponding to characteristic absorption of pure ZnO NCs. The absorption band edge shifts to 333 nm with increase of Mg content. Here ZnO is a direct band gap semiconductor. The optical band gaps of the samples were calculated using the following classical Tauc relation of optical absorption near band edge of the semiconductor:

$$(\alpha h\nu)^2 = C(h\nu - E_g) \qquad (5)$$

Where α is the optical absorption coefficient, hν is the incident photon energy, C is a constant. The band gap E_g was determined by plotting $(\alpha h\nu)^2$ as a function of hν and extrapolating the linear absorption edge of the curve to intersect the energy axis as shown in the Fig. 5b. The variation of band gap with dopant (Mg) concentration (x) is shown in the Fig. 5c indicating a linear behavior[42]. Therefore blue shifting of the band gap in Mg alloying ZnO NCs satisfies Vegard's law corresponding to band gap variation in semiconducting alloys. It can be inferred from the above discussion that band gap tuning of the $Zn_{1-x}Mg_xO$ NCs towards the higher energy is a consequence of Mg alloying.

Fig. S1b in ESI shows the absorbance spectrum of Ag@Ni core shell nanoparticles. Pure Ag NCs which were used as a core material show an LSPR band centred at 410 nm (ESI, Fig. S1 c) and Pure Ni particle shows a plasmon band near 330 nm according to the Mie's theoretical calculation[43]. The LSPR band for Ag@Ni core shell nanoparticles is blue shifted by 19 nm (absorption band centered at 391 nm) compare to pure Ag NCs

and also broadened. When two heterometals are in closer interparticle distance less than 2 nm there might be a plasmonic coupling between them. This can be a consequence of the overlapping of different plasmon modes such as capacitive plasmon mode and charge transfer plasmon mode[44,45]. In the reaction vessel Ni^{2+} ions got reduced by TOP and started to grow upon the surface of the Ag seeds and form Ag@Ni heterometallic system. Therefore due to the coupling of two plasmonic bands, the LSPR band of the core-shell structure is broadened and damped. In some research works such as Ag core/Au shell nanoparticle[46-48], the plasmon band is shifted towards the plasmon band of the shell material following the Mie's theory[49]. The presence of Ni shell shifts the plasmon band of Ag towards Ni plasmon band (lower wavelength)[50-52]. Therefore we can infer that the blue shifting of plasmon band in Ag@Ni system is due to the Ni shell formation upon Ag.

The exciton absorption of Ag@Ni/$Zn_{1-x}Mg_xO$ heterostructure as demonstrated in Fig 5(d) is almost similar to that of $Zn_{1-x}Mg_xO$. So Ag@Ni/$Zn_{1-x}Mg_xO$ heterostructure does not affect the band gap widening of the semiconductor. The most interesting observation is that the plasmon absorption wavelength of Ag@Ni core-shell structure (appeared at 391 nm) is found to be red shifted from 50 to 90 nm. There might be two possible reasons for such variation. Firstly it might be caused by the larger refractive index of the semiconductor surrounding the heterometal core-shell structure. This behavior is consistent with previous observations of plasmon shift to the higher wavelength i.e. lower energy in presence of high refractive index environment[53,54]. The LSPR frequency of metal NCs can be expressed as:

$$\omega_{sp} = \sqrt{\frac{\omega_p^2}{1+2\epsilon_m} - \gamma^2} \qquad (6)$$

Where ω_{sp} is the LSPR frequency, ω_p is the bulk plasmon frequency, ϵ_m is the dielectric constant of surrounding and γ is the damping factor. So an increase of dielectric constant of environment of metal NCs results in red shifting of LSPR band position. Dielectric constant of ZnO is much higher than TCE solvent[55]. Secondly the plasmon field of heterometalic core shell persists nearby surrounding and the heterostructure formation provides favorable condition for plasmon – exciton coupling and shifted the plasmon peak towards the higher wavelength. Since the Ag@Ni core-shell structure experiences two different dielectric media (one due to semiconductor and the other due to solvent) the LSPR peak is damped and broadened.

Photoluminescence property:

Photoluminescence (PL) property of ZnO NC upon Mg doping and Ag@Ni/$Zn_{1-x}Mg_xO$ heterostructure have been performed at room temperature. Figure 6 shows the PL profile in the range 350 nm to 650 nm of pure and alloyed NCs at excitation source 330 nm. ZnO having a highly ionic lattice, the valence band (VB) is composed of oxygen 2p orbital hybridized with Zn 3d states and conduction band (CB) composed of mainly Zn^{2+} excited states. So alloying with homovalent Mg^{2+} ion, not only change the valence band and conduction band structure as we already found a widening of band gap but also change the defect chemistry of ZnO. Normally the PL structure of ZnO NC (in any size) shows two types of emissions: (i) Near band edge emission (NBE) and (ii) Deep level emission. The PL profile of as-synthesized NCs shows a broad emission featuring with multiple humps in UV-VIS region. The emission profile is deconvoluted based on Gaussian distribution to achieve the multiple emission bands. The color of the deconvoluted curve depicts the color of emission in the particular region. Three sets of deconvulated peaks are obtained for all the samples. The peaks in UV region (370-410 nm) for pure ZnO are composed of the excitonic recombination. The excitonic recombination band is found to be gradually blue shifted with Mg^{2+} alloying from 384 nm to 353 nm similar to absorbance band due to increase of band gap with Mg^{2+} alloying. Several kinds of defects and vacancies are found to be responsible for the origin of broad band emission.[56] The defects states in ZnO can be generalised in two categories: (i) shallow trapped states which are closely situated to CB and are mainly composed of optical active zinc-related intrinsic defect states like zinc interstitial (Zn_i)[57] and zinc vacancy (V_{Zn}) (ii) deep trapped defect states like oxygen vacancy (V_0), oxygen interstitial (O_i), zinc vacancy, oxygen at zinc lattice site (O_{Zn}). Previous experimental results prove that Zn_i states are 0.22 eV below the CB[58]. So the violet and blue emissions at 395 nm and 416 nm for pure ZnO can be assigned as NBE and Zn_i levels emission. With increase in Mg^{2+} alloying the number of deconvulated peaks and relative intensity with respect to exciton recombination increases from 2 to 3 which indicates the formation of more Zn_i defects on Mg alloying along with band gap widening. The blue PL band may be originated for the recombination of photogenerated electrons in extended Zn_i states, which resides slightly below the normal Zn_i states[59] or the recombination of electrons from CB to oxygen interstitial site (O_i) which reside at much deeper level in band gap[60]. Although the formation energy of Zn_i is high but the recent study suggests that a non-equilibrium synthesis will accelerate the formation of Zn_i[59]. We found a non-equilibrium growth process during the synthesis of NCs as we described in TEM section. So the blue emission centred at 450 nm for pure ZnO NCs can be described as Zn interstitial or Zn interstitial-related complex defect[61]. All the alloyed NCs show a prominent blue emission band at 430 to 450 nm. Although the blue emission band has higher intensity than the excitonic recombination band for pure ZnO NC, but for 5% and 10% Mg doped ZnO NCs shows a relative lower intensity of blue emission than the excitonic recombination: might be a result of lesser concentration Zn_i defects states. The 20% and 30% Mg alloyed ZnO NCs shows higher probability of Zn_i to VB

recombination than band to band transition as evidenced from increase intensity of former one. The green emission band at 480 nm to 600 nm is deconvulated into three peaks for pure ZnO NCs. This broad green emission band may be due to (i) recombination of photo generated electrons in the conduction band with the deep state defect levels (V_o, V_{Zn}, O_i, Zn_i or O_{Zn} which is situated very close to the valence band) or (ii) recombination of electron in the shallow trap state (mainly Zn_i states) with the deep defect states. XPS analysis for ZnO and alloyed ZnO NCs (ESI, Fig. S14) shows the presence of oxygen vacancy and the O_i which appeared at lower binding energy than pure O 1s. So the oxygen vacancy related defects states like neutral (V_0), singly (V_0^+) or doubly ionized (V_0^{++}) states might be involved in luminescence process to generate the broad green emission. The intensity and broadness of green emission band centered at 490-500 nm region is found to be increased with increasing the Mg^{2+} alloying percentage and become maximum for 30% Mg alloyed ZnO NCs. The long tail beyond 550 nm may related to O_i defects as the literature study indicates O_i related PL peak appears at the higher wavelength region than the oxygen vacancy related emission[62,63]. So both the Zn_i and oxygen vacancy related defect states are found to be increased with Mg alloying up to 20% Mg alloyed sample except for 5% Mg alloyed NCs where Zn_i related PL got quenched. Strikingly all the PL intensity for 30% Mg alloyed NCs was found much lower compare to the other sample. Formation of amorphous MgO layer (which is concluded from TEM analysis) around the crystalline NC may be responsible for quenching the visible emission.

Fig. S15 in ESI shows the PL profile of Ag@Ni/$Zn_{1-x}Mg_xO$ NHSs with different amount of Mg^{2+}. The excitonic recombination band is found to be blue shifted with increase Mg^{2+} alloying as we observed for pure $Zn_{1-x}Mg_xO$ NCs. Blue emission related to recombination of electrons in shallow trap Zn_i states to CB are present for all the heterostructures. The visible emission beyond 450 nm is found to be quenched for all the heterostructure NCs. This indicates a decrease in electron-hole recombination through defect derived states. Metal NCs are epitaxially connected with $Zn_{1-x}Mg_xO$ NCs/nanoflowers as confirmed from TEM analysis and may act as an electron sink. So the photoexcited electrons may prefer to go metal site. Scheme I shows a relative band alignment of Ag and ZnO. From the literature study[64], the Fermi energy (E_F) level of Ag (E_F = -4.7 eV) is found to be 0.9 eV below the conduction band edge of ZnO. We found the Zn_i related PL for all heterostructure as it reside 0.22 eV below of CB and above the E_F of Ag. So upon excitation with 330 nm, the photoexcited electron in CB can decay through Zn_i defect state to VB giving the blue emission or may transfer to Ag metal. The oxygen vacancy related defect states are the deep trap states lying much below the E_F of Ag. So there is a lower probability of recombination of electron to V_0 , V_0^+ or V_0^{++} states and results in diminution or quench of green emission. The probable decay paths for heterostructures are schematically presented in Scheme I. Therefore, metal nanoparticle attachment is very beneficial to transfer photoexcited electrons of $Zn_{1-x}Mg_xO$ to Ag.

Photocatalytic activity:

Prior to photocatalytic activity test the ligands were removed by a ligand exchange process followed by thermal annealing. Oleylamine was first replaced by n-butyl amine then the washed NCs were annealed at 250 °C to remove organic part completely. The change of RhB dye concentration was monitored by measuring the optical absorbance at 553 nm of the suspension at 30 min time interval for only alloyed ZnO NCs and 5 min time interval for Ag@Ni/$Zn_{1-x}Mg_xO$ heterostructure (as this material shows high photocatalytic activity) respectively. To compare the photo reduction rate of RhB in presence of different catalyst, we plotted C/C_0 vs. t as depicted in Fig. 7, where C_0 is the concentration of dye at equilibrium established at dark condition and C is the concentration of nondegraded dye after different time intervals of irradiance. The photodegradation of RhB in the presence of pure ZnO was relatively slow, with 60% of RhB degraded after an illumination time of 90 min (Fig. 7a). Whereas nearly 77%, 88% and 98% RhB was found to be photo degraded in presence of 5%, 10% and 20% Mg alloyed ZnO sample respectively in 90 min. We found a decrease in degradation rate for 30% Mg alloyed ZnO sample in similar condition where only 90% RhB was found to degraded. The photoreduction kinetics of RhB follows a pseudo first order, expressed by, $\ln (C_0/C) = Kt$, K is the apparent rate constant. Fig. 7b shows plot of $\ln(C_0/C)$ vs t for ZnO and $Zn_{1-x}Mg_xO$ samples. $Zn_{0.8}Mg_{0.2}O$ sample has the highest rate constant value of 0.062 min^{-1} which is nearly ~ 3.5 times higher than that of pure ZnO (k_1 = 0.018 min^{-1}). The increase of photocatalytic activity can be attributed for two reasons: (i) Mg alloying which increases the conduction band potential value making the system more reducing, (ii) change of morphology on Mg alloying. On Mg increasing the shape of NCs was found to be change from pyramid to roughed surface hexagonal base self assembled crown shaped and finally to hierarchical shaped nanoflower. So on Mg alloying the surface area of NCs increases which results in an increase of dye adsorption on NC surface. Flower shape morphology was found to be lost (from TEM analysis) for 30% Mg alloyed ZnO which gives rise to a decrease in catalytic activity than 20% alloyed sample.

The effect of metal-semiconductor heterostructure on photocatalytic activity has been shown in right panel of Fig. 7c and d. At only 60 min of irradiance, 80% of RhB was found to be degraded in presence Ag@Ni/ZnO catalyst. Nearly 92%, 95% and 99% of RhB was degraded in presence of 5%, 10% and 20% Mg alloyed metal-semiconductor heterostructure. The maximum photodegradation rate constant value was found for Ag@Ni/$Zn_{0.8}Mg_{0.2}O$ catalyst with value 0.07 min^{-1} which is

higher than the non-metal decorated counterpart. Metal decorated $Zn_{0.7}Mg_{0.3}O$ does not show a sharp decrease in rate constant value like pure $Zn_{0.7}Mg_{0.3}O$ sample. The rate constant value is found to be 0.068 min^{-1} much similar to $Ag@Ni/Zn_{0.8}Mg_{0.2}O$ sample. The sheet like morphology of $Ag@Ni/Zn_{0.7}Mg_{0.3}O$ [ESI, Fig. S9] and decorated with multiple metal dots with large exposed surface area adsorb dye compound in higher amount compared to $Zn_{0.7}Mg_{0.3}O$ sample. All the metal decorated catalyst was found to be magnetically separable by small magnet bars depicted in Fig. S17 in ESI. Fig. S20 in ESI depicts the TEM image of recovered photocatalysts after one photocatalytic cycle which shows the coexistence of metal-semiconductor in a single nanoflower. The change of absorbance of dye in presence of catalyst has been shown in ESI (Fig. S18).

To access better understanding of photocatalytic property enhancement with morphological change on Mg alloying we have performed Brunauer–Emmett–Teller (BET) gas sorption measurements. The nitrogen adsorption/desorption isotherms and the pore size distribution plots of different Ag@Ni decorated $Zn_{1-x}Mg_xO$ systems are shown in Fig. S19 in ESI. The estimated BET specific surface area and pore size of samples are listed in Table 1. The typical type IV nature of the curves and hysteresis loop indicates the presence of mesoporous nature of as-synthesis heterostructured materials according to the IUPAC classification. The BET surface area for Ag@Ni/ZnO is found to be 18.21 m^2/g. The Barrett–Joyner–Halenda (BJH) pore size distribution curve indicates non-uniformity of pores in the range 1 to 15 nm with high population density at 1.5 nm and 3 nm. This distribution of pore size is for non-uniform size of ZnO nanopyramids in heterostructures and presence of rough surfaces in ZnO as also observed from TEM analysis (Fig. 3(a)). The BET surface area increases with Mg alloying in heterostructures and the value obtained for $Ag@Ni/Zn_{0.9}Mg_{0.1}O$ and $Zn_{0.8}Mg_{0.2}O$ heterostructure are 31.26 m^2/g and 38.32 m^2/g. This increment of surface area can be attributed to increase in oriented attachment which leads to self assembled nanoflower formation on Mg alloying. Higher pore size contribution in pore size distribution is found to be increase with Mg alloying particularly for $Ag@Ni/Zn_{0.8}Mg_{0.2}O$ where the contribution of pore size ~ 5 nm to 15 nm is higher than other samples. Formation of multipetal multilayer nanoflower (Fig. 4(b)) for $Ag@Ni/Zn_{0.8}Mg_{0.2}O$ sample is the main reason for increase in pore size. Nanoflower morphology, high surface area and pore size assist the faster dye degradation.

Photoresponse property:

To utilize the enhanced photo efficiency of the as - synthesized metal-semiconductor heterostructure, we fabricated a photo detector device using these materials. Figure 8 shows the photoresponse curve for all the samples at bias voltage of 5 volt in presence of light irradiance of 0.65 W/cm^2 power densities with 40 sec time lapse. The yellow shaded area shows current in presence of light and other shows in absence of light. The photocurrent gain which is the ratio of current in presence and absence of light ($I_{Photon} : I_{Dark}$) is found to be low for Ag@Ni/ZnO system with a value of 11 and maximum for $Ag@Ni/Zn_{0.7}Mg_{0.3}O$ system with a value of 230. Mg alloying in Ag@Ni/ZnO system increases the photocurrent value as similar to photocatalysis phenomenon except for the $Ag@Ni/Zn_{0.7}Mg_{0.3}O$ composition which reveals the most responsive device in spite of poor photocatalytic activity than $Ag@Ni/Zn_{0.8}Mg_{0.2}O$. This suggests that probably morphology of NCs does not affect photoresponse property of material. Mg alloying also has a striking effect on the current gain and decay nature during the repetitive photoresponse measurement. The pure Ag@Ni/ZnO system shows a slow gain and slow decay of photocurrent. Incomplete separation of electron-hole pair upon exposure to light and decay of photoexcited electrons through trap/defects states during DARK condition may result in slow response nature. For the fabrication of a fast and stable photodetector, two major criteria are to be fulfilled: (i) increase of lifetime of exciton pair, i.e. complete separation of e^- and h^+, and (ii) fast recombination of e^- and h^+ pair in absence of light. These two criteria have been achieved for $Ag@Ni/Zn_{0.7}Mg_{0.3}O$ system where maximum photocurrent gain value (~ 230) is found. Moreover, the photocurrent gain and decay patterns appear to be relatively faster compare to other devices. Number of metal NCs situated with each semiconductor NCs/nanoflower is found to be crucial in order to get fast responsive device. The pure ZnO NCs are situated with one or two metal NCs whereas the nanoflowers ($Zn_{1-x}Mg_xO$, x = 0.05, 0.1, 0.2) and specially the nanosheets (x = 0.3) are found to be situated with three or more metal NCs which increases the photon absorbance efficiency of each nanoflower through LSPR and gives rise to efficient charge separation.

For better understanding of individual contribution of band gap exciton of $Zn_{1-x}Mg_xO$ and plasmon absorbance of Ag@Ni on photochemical and photophysical properties of $Ag@Ni/Zn_{0.8}Mg_{0.2}O$ NHS, we have performed the photocatalytic and photoresponse properties using a cut-off filter at 390 nm. From both the experiments (ESI, Fig. S21) we have found that photoactivity is maximum under Xenon light irradiance and minimum in presence of visible light (> 390 nm). UV excitation gives the intermediate value of rate constant of dye degradation and photocurrent gain. When the NHSs were excited only by visible light, NHSs absorbs light by plasmonic excitation of Ag@Ni metal particles. Plasmon induced excited electrons of Ag@Ni do not have sufficient energy to overcome Schottky barrier between metal and semiconductor. This results in poor photoactivity of NHS only under visible light. UV band gap excitation of $Zn_{1-x}Mg_xO$ generates electrons which can easily transfer to Ag@Ni, preventing electron-hole recombination. Thus the separation of photogenerated charge carriers can promote photoacitivity. Synergetic effect of

excitation of plasmon of metal and band gap exciton of semiconductor under Xenon light illumination gives rise to the highest photoactivity. Plasmonic nanostructures can induce hot electron transfer, increase absorption coefficient and enhance local electric field.[32,41,65,66,67] Electromagnetic field enhancement predominates when palsmonic resonance and band gap exciton wavelengths overlap.[68,69] Palsmonic absorbtion wavelength (391 nm) of Ag@Ni is very close to band gap exciton (333-362 nm) of $Zn_{1-x}Mg_xO$. This suggests that increase of local electric is the major contributor to significant increase of photocatalyic activity and photoresponse property.

Magnetic property:

Magnetization as function of temperature and magnetic field of Ag@Ni/ZnO NHSs was studied using superconducting quantum interference device (SQUID) magnetometer (Quantum Design MPMS, XL Evercool model). Zero field cooled (ZFC) and field cooled (FC) magnetizations with temperature are displayed in Fig. 9a. A bifurcation between ZFC and FC curves occur at about 50 K. The ZFC magnetization reveals a prominent peak around 27 K known as blocking temperature (T_B). The value of T_B depends on the volume of magnetic phase. An extremely smaller value of T_B compared to Curie temperature (627 K) of bulk Ni suggests that the thickness of Ni shell is very small. Magnetization vs. magnetic field (M-H) curves at 300 K and 5 K are depicted in Fig. 9b. At low temperature (5 K) M-H curve clearly exhibits hysteresis loop. The estimated coercivity at 5 K is 101 Oe. An absence of hysteresis loop at 300 K indicates zero coercivity. The characteristic features of temperature dependent magnetization and M-H curves imply that the magnetic heterostructure is ferromagnetic below T_B and is superparamagnetic above T_B. Such kind of magnetic behavior is very useful to isolate the magnetic heterostructure from solution by a small magnet at room temperature.

Conclusion:

In summary we successfully synthesized monodispersed ZnO and Mg alloyed ZnO nanostructures with solid solubility limit ~ 30%. The morphological change of ZnO from nanopyramid to hierarchical shape with intact colloidal stability and well dispersed nature on Mg alloying has been explained based on oriented attachment process. Mg alloying increases both the shallow trap and deep trap defect concentration in ZnO system. Magnetc plasmonic metal - semiconductor NHS has been successfully synthesized using Ag@Ni as metal seed particle. Minimum lattice mismatch between periodic arrangement of 2 (111) plane of Ag with 3 (110) planes of ZnO leads to an epitaxial growth of $Ag@Ni/Zn_{1-x}Mg_xO$ heterostructure. Efficient epitaxy formation and Mg alloying increase the photoactivity of ZnO. A potent photocatalyst and fast response photodetector has been fabricated with $Ag@Ni/Zn_{0.8}Mg_{0.2}O$ and $Ag@Ni/Zn_{0.7}Mg_{0.3}O$ NHS. Superparamagnetism has been found for Ag@Ni seeds which makes the photocatalyst magnetically separable.

Acknowledgment:

The authors S. Paul and S. Ghosh sincerely acknowledge DST INSPIRE fellowship and CSIR, India respectively for providing the fellowship during the tenure of the work.

Notes and references

1. R. S. Selinsky, Q.Ding, M. S. Faber, J. C. Wright and S. Jin, *Chem. Soc. Rev.,* 2013, **42**, 2963-2985.
2. A. Vaneski, A. S. Susha, J. Rodríguez-Fernández, M. Berr, F. Jäckel, J. Feldmann and A. L. Rogach, *Adv. Funct. Mater.* **2011**, *21*, 1547–1556.
3. R. S. Selinsky, Q. Ding, M. S. Faber, J. C. Wright and S. Jin, *Chem. Soc. Rev.,* 2013, **42**, 2963-2985.
4. S. J. Pearton, D. P. Norton, and F. Ren, *small*, 2007, **3**, 1144 – 1150.
5. Q. Lu, Z. Lu,Y. Lu, L. Lv, Y. Ning, H. Yu, Y. Hou and Y. Yin, *Nano Lett.,* 2013, **13**, 5698−5702.
6. S. Ghosh, M. Saha, S. Paul and S. K. De, *Nanoscale*, 2015, **7**, 18284–18298.
7. M. N. Tahir, F. Natalio, M. A. Cambaz, M. Panth¨ofer, R. Branscheid, U. Kolb and W. Tremel, *Nanoscale*, 2013, **5**, 9944–9949.
8. V. Etacheri, R. Roshan and V. Kumar, *ACS Appl. Mater. Interfaces* 2012, **4**, 2717−2725.
9. N. Zhou, L. Polavarapu, N. Gao, Y. Pan, P. Yuan, Q. Wang and Q. Xu, *Nanoscale*, 2013, **5**, 4236–4241.
10. B. K. Patra, A. K. Guria, A. Dutta, A. Shit and N. Pradhan, *Chem. Mater.,* 2014, **26**, 7194−7200.
11. X. Yu, A. Shavel, X. An, Z. Luo, M. Ibáñez and A. Cabot, *J. Am. Chem. Soc.,* 2014, **136**, 9236−9239.
12. S. Ghosh, M. Saha and S. K. De, *Nanoscale*, 2014, **6**, 7039-7051.
13. M. Saha, S. Ghosh, V. D. Ashok and S. K. De, *Phys. Chem. Chem. Phys.,* 2015, **17**, 16067—16079.
14. J. Chang and E. R. Waclawik, *CrystEngComm*, 2012, **14**, 4041–4048.
15. J. Li, H. Fan and X. Jia, *J. Phys. Chem. C*, 2010**, 114**, 14684–14691.
16. Y. Jin, J. Wang, B. Sun, J. C. Blakesleyand N. C. Greenham, *Nano Lett.,* 2008, **8**, 1649-1653.
17. N. Gogurla, A. K. Sinha, S. Santra, S. Manna, and S. K. Ray, *Sci Rep.,* 2014; **4**, 6483-6492.
18. M. Shim, A. Javey, N. W. S. Kam and H. Dai, *J. Am. Chem. Soc.*, 2001, **123**, 11512-11513.
19. W. K. Liu, K. M. Whitaker, K. R. Kittilstved and D. R. Gamelin, *J. Am. Chem. Soc.,* 2006, **128**, 3910−3911.
20. W. K. Liu, K. M. Whitaker, A. L. Smith, K. R. Kittilstved, B. H. Robinson and D. R. Gamelin, *PRL*, 2007, **98**, 186804-186804.
21. A. W. Cohn, K. R. Kittilstved and Daniel R. Gamelin, *J. Am. Chem. Soc.,* 2012, **134**, 7937−7943.
22. X. Qiu, L. Li, J. Zheng, J. Liu, X. Sun, and G. Li, *J. Phys. Chem. C*, 2008, **112**, 12242.
23. X. D. Zhang, M. L. Guo, C. L. Liu, L. A. Zhang, W. Y. Zhang, Y. Q. Ding, Q. Wu and X. Feng, *Eur. Phys. J. B*, 2008, **62**, 417-421.
24. R. D. Shannon, Acta Crystallogr. Sect. A: Foundations 1976, 32,751−767.
25. A. Ohtomo, M. Kawasaki, T. Koida, K. Masubuchi, H. Koinuma, Y. Sakurai, Y. Yoshida, T. Yasuda, and Y. Segawa, *Appl. Phys. Lett*., 1998, **72**, 2466-2468.

26. S. C. Su, Y. M. Lu, Z. Z. Zhang, C. X. Shan, B. H. Li, D. Z. Shen, B. Yao, J. Y. Zhang, D. X. Zhao, and X. W. Fan, *Appl. Phys. Lett.,*2008, **93**, 082108-082111.
27. J. W. Chiou, H. M. Tsai, C. W. Pao, K. P. Krishna Kumar, S. C. Ray, F. Z. Chien, W. F. Pong, M. H. Tsai, C. H. Chen, H. J. Lin, J. J. Wu, M.-H. Yang, S. C. Liu, H. H. Chiang, and C. W. Chen, *Appl. Phys. Lett.,* 2006, **89**, 043121-043124.
28. N. Zhang, X. Wang, Z. Ye and Y. Jin, *SCIENTIFIC REPORTS*, 2014, **4**, 4353-4360.
29. Y. Yang, Y. Jin, H. He, Q. Wang, Y. Tu, H. Lu, and Z. Ye, *J.* Am. Chem. Soc., 2010, **132**, 13381–13394.
30. P. Li, Z. Wei, T. Wu, Q. Peng and Y. Li, *J. Am. Chem. Soc.,* 2011, **133**, 5660–5663.
31. Y. Chen, D. Zeng, K. Zhang, A. Lu, L. Wang and D. L. Peng, *Nanoscale*, 2014, **6**, 874–881.
32. X. Zhang, Y. L. Chen, R. S. Liu and D. P. Tsai, *Rep. Prog. Phys.,* 2013, **76,** 046401-046442.
33. H. Guo, Y. Chen, X. Chen, R. Wen, G. H. Yue and D. L. Peng, *Nanotechnology*, 2011, **22,** 195604-195612.
34. S. Sharma, B. Kim, and D. Lee, *Langmuir* 2012, **28**, 15958.
35. Elements of X-ray Diffraction, B. D. Cullity, Addision-Wesley Pub. Comp. Inc. 1956
36. Powder Diffraction ed. by R. E. Dinnebier and S. J. L. Billinge, RSC Publishing, 2008
37. S. Ghosh, K. Das, G. Sinha, J. Lahtinen and S. K. De, *J. Mater. Chem. C*, 2013, 1, 5557–5566.
38. D. A. Schwartz, N. S. Norberg, Q. P. Nguyen, J. M. Parker and D. R. Gamelin, J. Am. Chem. Soc*.,* 2003, **125**, 13205-13218
39. O. K. Ranasingha, C. Wang, P. R. Ohodnicki, Jr., J. W. Lekse, J. P. Lewisab and C. Matranga, *J. Mater. Chem. A*, 2015, **3**, 15141–15147.
40. M. Grzelczak, B. Rodríguez-González, J. Pérez-Juste and L. M. Liz-Marzán, *Adv. Mater.,* 2007, **19**, 2262–2266.
41. S. K. Dutta, S. K. Mehetor and N. Pradhan, *J. Phys. Chem. Lett*., 2015, **6**, 936−944.
42. J. Singh, P. Kumar, K. S. Hui, K. N. Hui, K. Ramam, R. S. Tiwaria and O. N. Srivastava, *Cryst Eng Comm*, 2012, **14**, 5898-5904.
43. J. A. Creighton and D. G. Eadont, *J. Chem. Soc. FaradayTrans*., 1991, **87**, 3881-3891.
44. J. Lee, M. You, G. Kim, and J. Nam, *Nano Lett.* 2014, **14**, 6217−6225.
45. S. Ghosh, S. Khamarui, M. Saha and S. K. De, *RSC Adv*., 2015, **5**, 38971–38976.
46. D. Chen and C. Chen, *J. Mater. Chem.,* 2002, **12**, 1557–1562.
47. H. Jiang, T. Akita, T. Ishida, M. Haruta, and Q. Xu, *J. Am. Chem. Soc.,* 2011, **133**, 1304–1306.
48. A. Henglein, *J. Phys. Chem. B,* 2000**, 104***,* 2201-2203.
49. H. Xu, *Phys Rev B*, 2005,**72**, 073405.
50. Z. Zhang, T. M. Nenoff, J.Y. Huang, D. T. Berry and P. P. Provencio, *J. Phys. Chem. C,*2009, **113***,* 1155–1159.
51. M. Gaudry, E. Cottancin, M. Pellarin, J. Lerme´, L. Arnaud, J. R. Huntzinger, J. L. Vialle, M. Broyer, J. L. Rousset, M. Treilleux and P. Me´linon, *Phys Rev B*,2003, **67**, 155409-155419.
52. E. Cottancin, M. Gaudry, M. Pellarin, J. Lerm´e, L. Arnaud, J.R. Huntzinger, J.L. Vialle, M. Treilleux, P. M´elinon, J. L. Rousset, and M. Broyer, *Eur. Phys. J. D*,2003, **24**, 111–114.
53. J. Lee, E. V. Shevchenko, and D. V. Talapin, *J. AM. CHEM. SOC.*, 2008, **130**, 9673–9675.
54. E. Shaviv, O. Schubert, M. Alves-Santos, G. Goldoni, R. D. Felice, F. Vallee, N. D. Fatti, U. Banin, and C. Sonnichsen, *ACS Nano*, 2011, **5**, 4712-4719.
55. Y. Yang, W. Guo, X. Wang, Z. Wang, J. Qi and Y. Zhang, *Nano Lett.*, 2012, **12**, 1919–1922.
56. A. Janotti and C. G. Van de Walle, *Phys Rev B*, 2007,**76**, 165202 -165224.
57. Bixia Lin, Zhuxi Fu and Yunbo Jia, *Appl. Phys. Lett.*, 2011, **79**, 943-945.
58. E. G. Bylander, *J. Appl. Phys.* 1978, **49**, 1188.
59. H. Zeng, G. Duan, Y. Li, S. Yang, X. Xu, and W. Cai, *Adv. Funct. Mater.,* 2010, **20**, 561–572.
60. L. Han, L. Cui,W. Wang, J. Wang and X. Du, *Semicond. Sci. Technol.*,2012, **27,** 065020-065028.
61. D. C. Look, G. C. Farlow, P. Reunchan, S. Limpijumnong, S. B. Zhang and K. Nordlund, *Phys. Rev. Lett.*,2005, **95,** 225502-225506.
62. S. S. Kurbanov , G. N. Panin , T. W. Kim and T. W. Kang, *Journal of Luminescence.*, 2009, **129**, 1099–1104.
63. J. W. P. Hsu, D. R. Tallant, R. L. Simpson, N. A. Missert and R. G. Copeland, *Appl. Phys. Lett.*,2006, **88**, 252103-252106.
64. Y. Zheng, L. Zheng, Y. Zhan, X. Lin, Q. Zheng and K. Wei, *Inorg. Chem.,* 2007, **46**, 6980-6986.
65. Ji Won Ha, T. Purnima A. Ruberu, Rui Han, Bin Dong, Javier Vela, and Ning Fang, *J. Am. Chem. Soc*., 2014, **136**, 1398−1408
66. C. Clavero, *Nature Photonics*, 2014, **8,** 95 -103
67. K. Wu, William E. Rodríguez-Córdoba, Ye Yang, and T. Lian, *Nano Lett*., 2013, **13**, 5255−5263
68. Z. Chen, L. Fang, W. Dong, F. Zheng, M. Shenaand Junling Wang, *J. Mater. Chem. A*, 2014, **2**, 824-832
69. Scott C. Warren and E. Thimsen., *Energy Environ. Sci.,* 2012, **5**, 5133-5146

Table 1: BET surface area and total pore volume of samples

Sample	S_{BET} (m^2g^{-1})	Pore size distribution (nm)
Ag@Ni/ZnO	18.21	1 to 15
Ag@Ni/$Zn_{0.9}Mg_{0.1}O$	32.26	2.5 to 20
Ag@Ni/$Zn_{0.8}Mg_{0.2}O$	38.32	2.5 to 25

Figure Caption:

Fig.1: XRD pattern of pure and Mg(II) alloyed ZnO ($Zn_{1-x}Mg_xO$) nanocrystals upto x= 0.5. Impurity peaks related to cubic MgO appear at x=0.4 sample.

Fig.2: (a-c) Large area TEM, HRTEM and SAED pattern of a single nanocrystal along c-axis respectively. Inset of (a) shows the tilted view of a nanocrystal. (d-f) Large area TEM, HRTEM and SAED of 10 mol% Mg alloyed ZnO self-assembled nancrystal. Inset of (d) shows the tilted view of self assembly. (g and h) TEM and HRTEM of 20 mol% Mg alloyed ZnO multipetal nanoflower. (i) FFT pattern of yellow squared area in Fig.2h shows the presence of twin (010) and (020) planes.(j-k) Large area and closer view 30 mol% Mg alloyed ZnO shows the decrease of assembly size.(l) HRTEM of that shows the presence of (002) planes. (m-o) TEM, HRTEM and FFT of 40 mol% Mg alloyed ZnO shows a high decrease of particle size.

Fig. 3: (a) TEM image of Ag@Ni/ZnO NHS. (b) HRTEM image of NHS at the site of interest. (c) FFT pattern of yellow squared area, the pure ZnO region. (d) Reconstructed HRTEM image shows the presence of (110) and (102) planes of ZnO. (e) FFT pattern of orange squared area: interface region. The highlighted spots shows the same direction of growth of Ag(111) and (110) of ZnO. (f) Reconstructed HRTEM image by masking the white and cyan circled spots in FFT pattern showing the minimal lattice mismatch between Ag (111) and (110) of ZnO planes.

Fig. 4: (a) Large area TEM image of $Ag@Ni/Zn_{0.8}Mg_{0.2}O$ NHS. (b) Inverted bright field TEM image of same shows the nanoflower morphology of alloyed semiconductor connected with multiple metal core-shell dots. (c) A closer view of the sample. (d) HRTEM image of a part of NHS shows the connectivity of metal part with alloyed semiconductor. (e) FFT pattern of orange squared area, the interface of Ag and ZnO of Fig. 4d shows the same direction of Ag(111) and ZnO (012) planes. (f) Reconstructed HRTEM image by masking the white and cyan color spots in FFT pattern. (g) FFT pattern of yellow squared area of Fig. 4d showing the presence of twin (012) and (020) planes of ZnO. (h) reconstructed HRTEM image from FFT shows the presence of dislocation.

Fig. 5: (a) Absorbance spectra of pure ZnO and $Zn_{1-x}Mg_xO$ nanocrystals. The absorbance edge shifts toward lower wavelngth on Mg alloying. (b) Tauc plot of different sample showing the change of band gap. (c) Change of band gap with x. (d) Absorbance spectra of different $Ag@Ni/Zn_{1-x}Mg_xO$ NHS. Transparent green area depicts the plasmonic absorbance of metal part and blue region depicts the band gap absorbance of $Zn_{1-x}Mg_xO$.

Fig. 6: (a-e) PL emission profile of different $Zn_{1-x}Mg_xO$ nanocrystals, where x varies from 0 to 0.3.

Fig. 7: (a-b) Light driven photodegradation of RhB dye in presence of alloyed ZnO nanocrystals. (c-d) The same in presence of different $Ag@Ni/Zn_{1-x}Mg_xO$ NHS.

Fig. 8: Temporal photoresponse of different $Ag@Ni/Zn_{1-x}Mg_xO$ NHS. Right panel shows photocurrent gain value.

Fig. 9: (a) Magnetization vs. temperature (M-T) plot of Ag@Ni/ZnO NHS at H = 100 Oe. (b) Magnetization vs. magnetic field (M-H) plot at 5 K and 300 K. Inset shows the presence of distinct hysteresis loop at 5 K.

Scheme-I: Relative band alignment of Ag and $ZnO/Zn_{1-x}Mg_xO$ and probable transition in heterostructure.

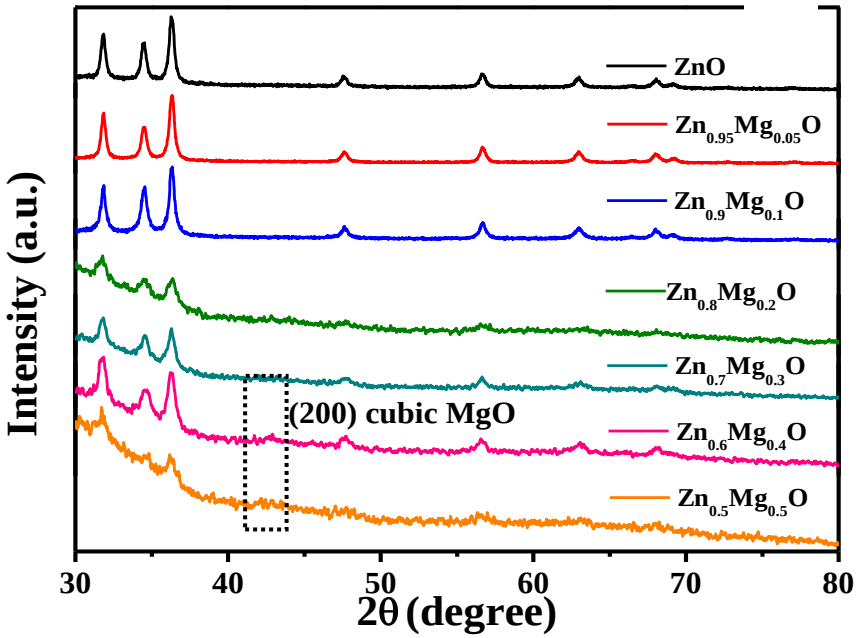

Fig. 1.

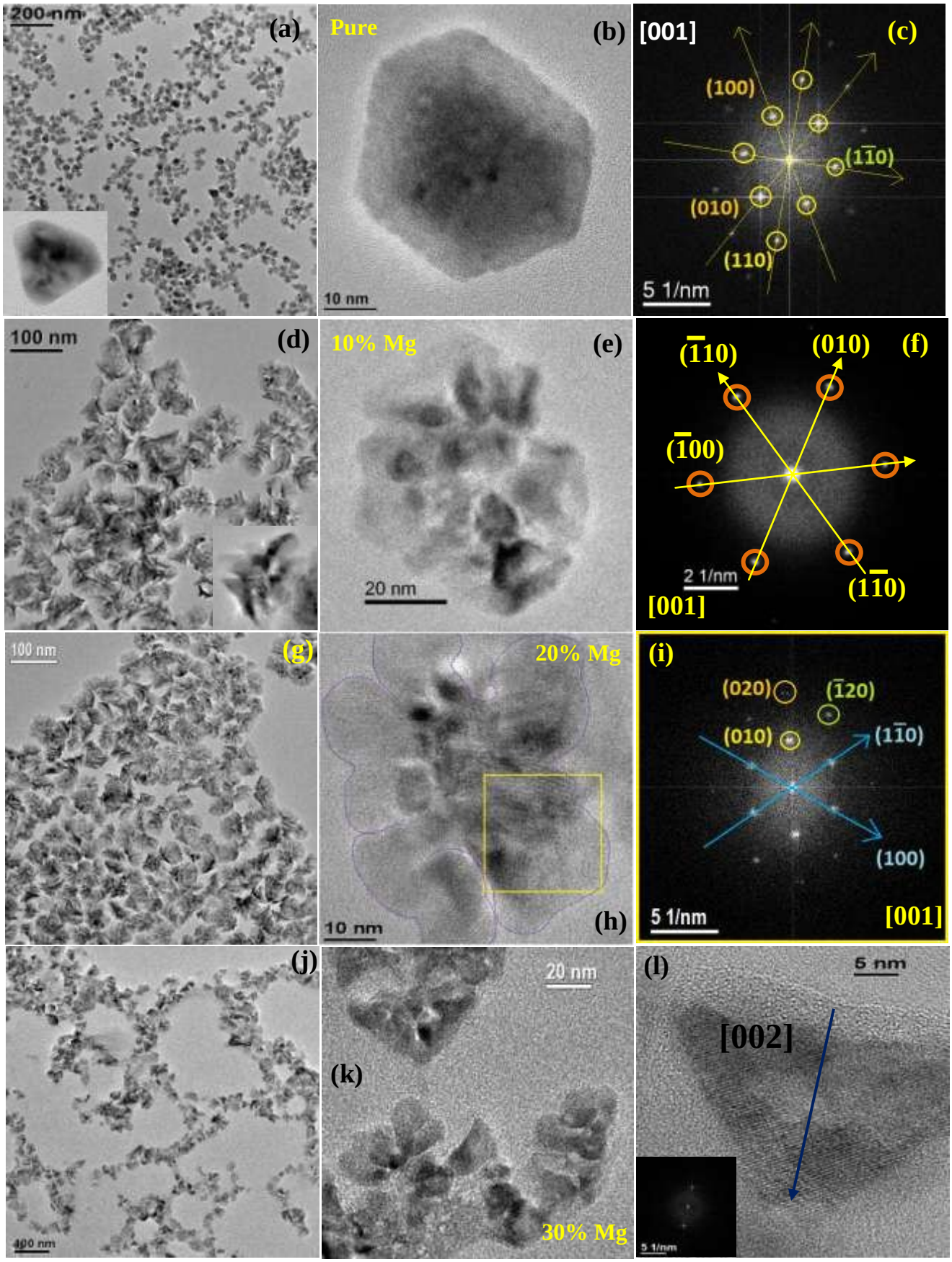

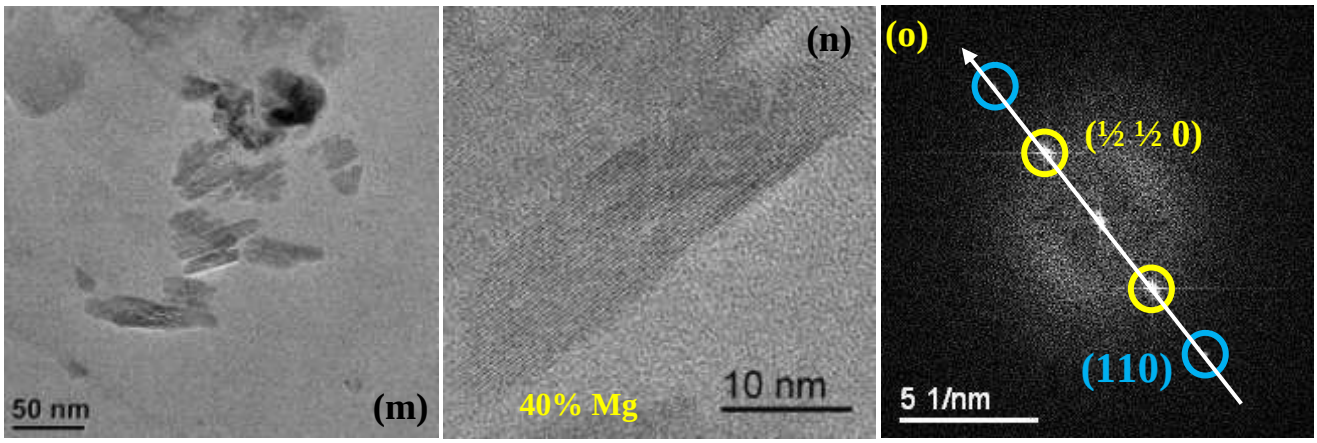

Fig. 2.

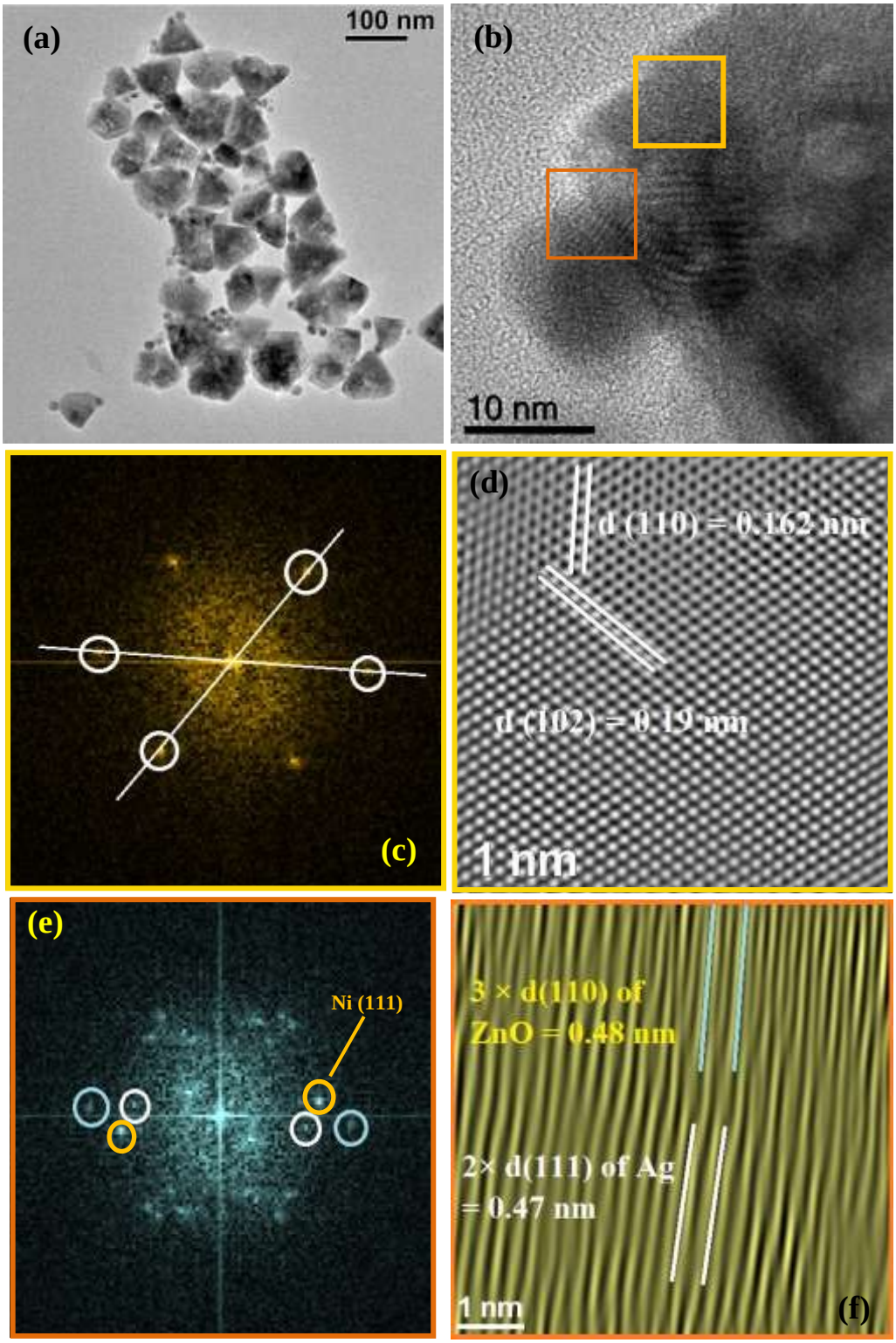

Fig. 3.

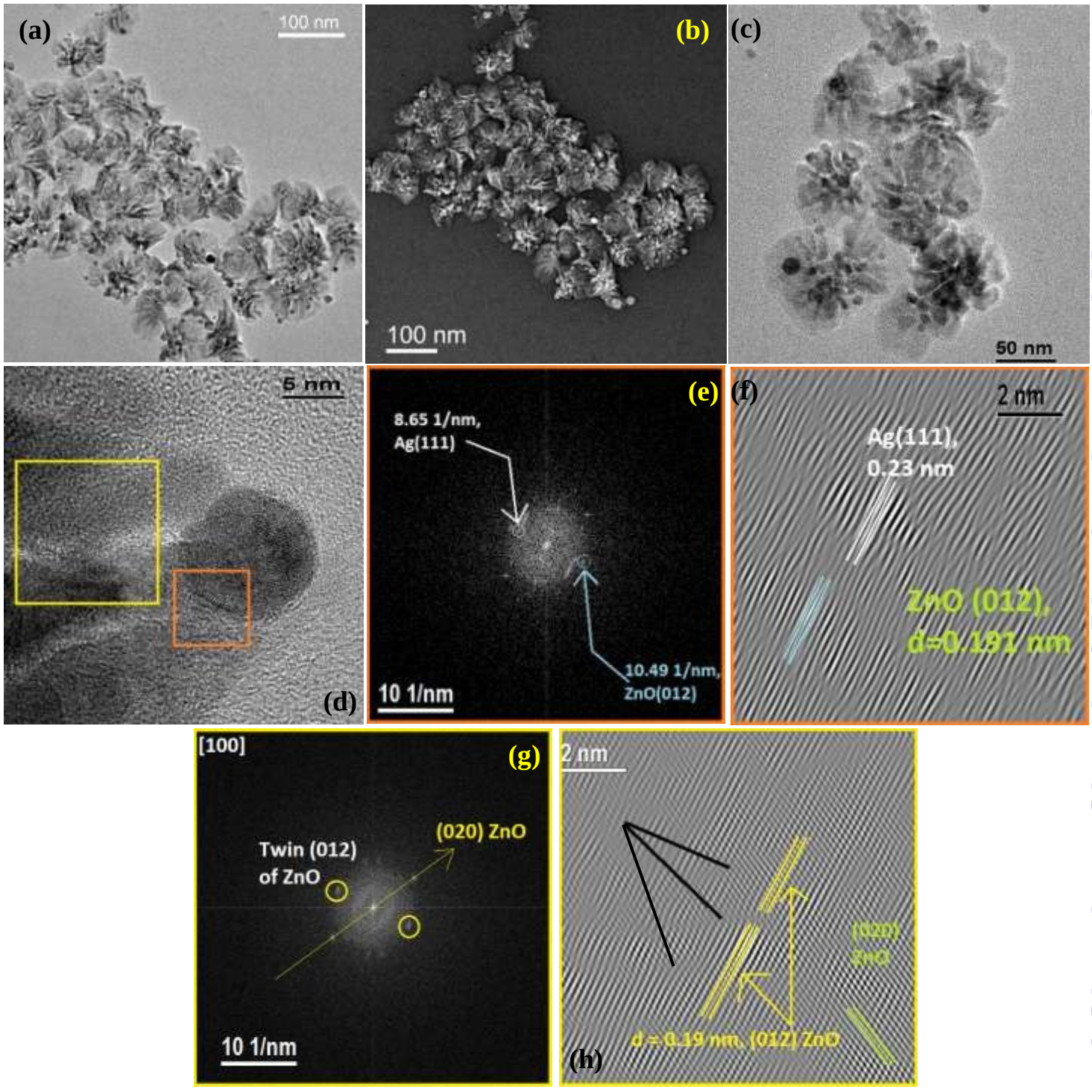

Fig. 4.

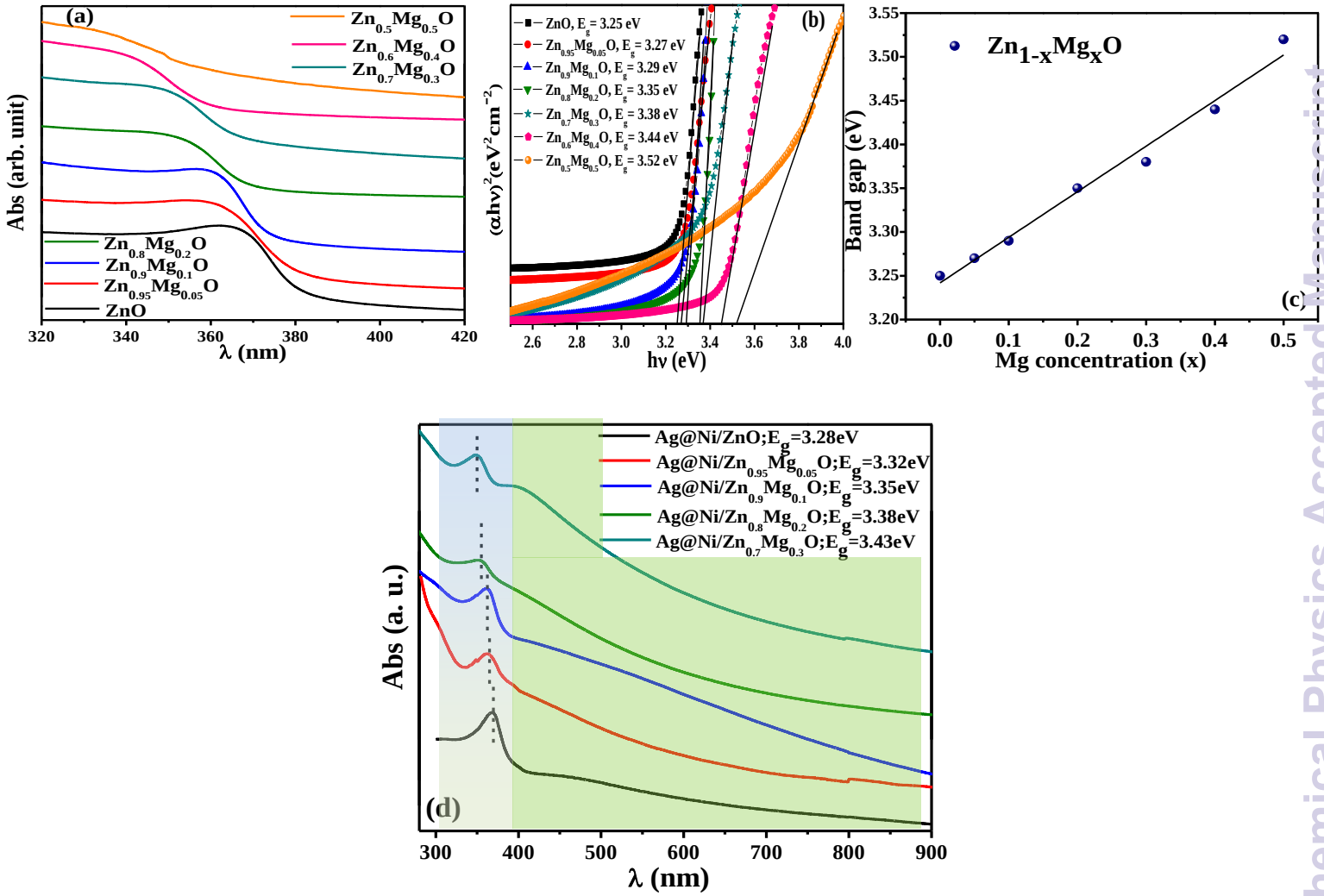

Fig. 5.

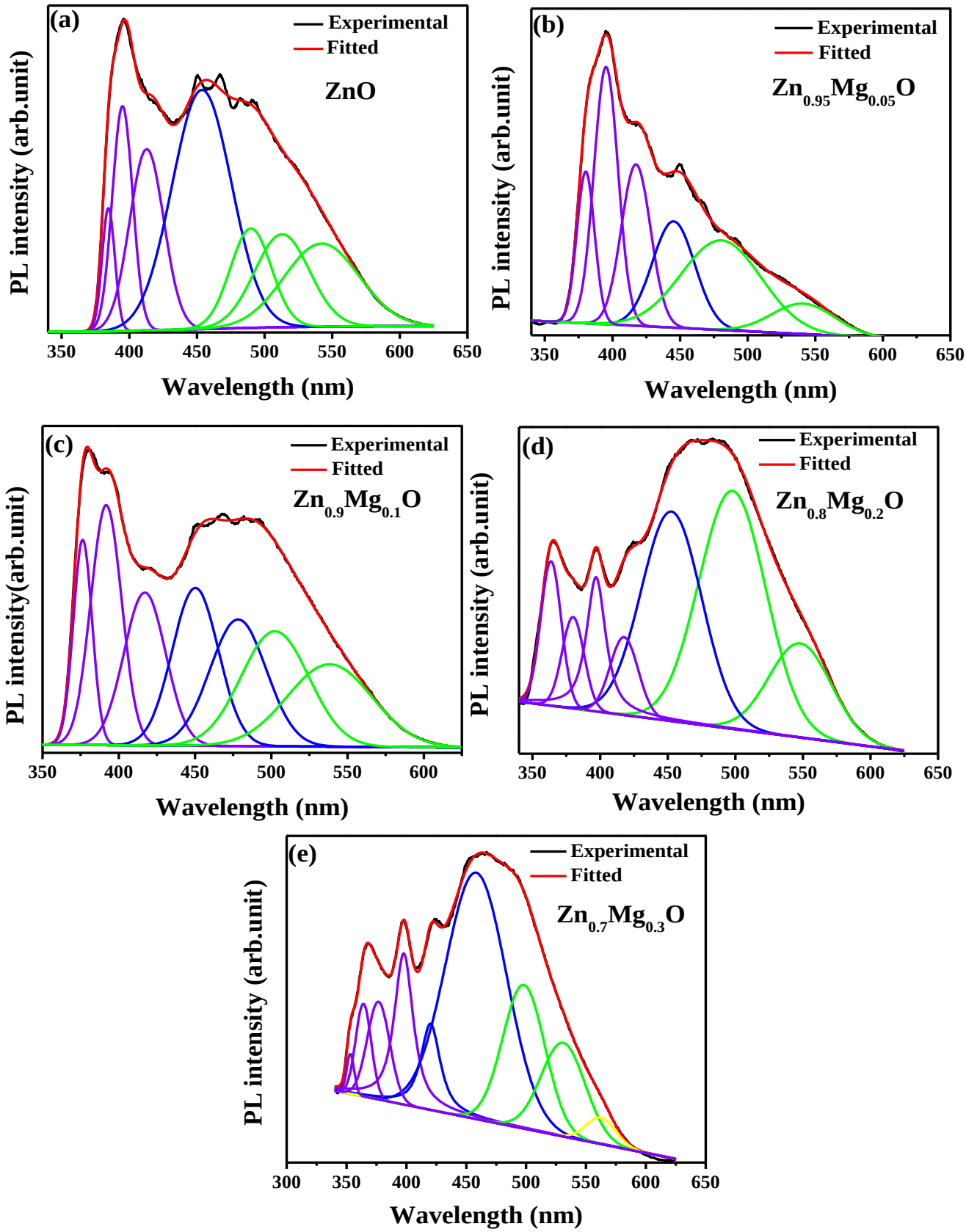

Fig. 6.

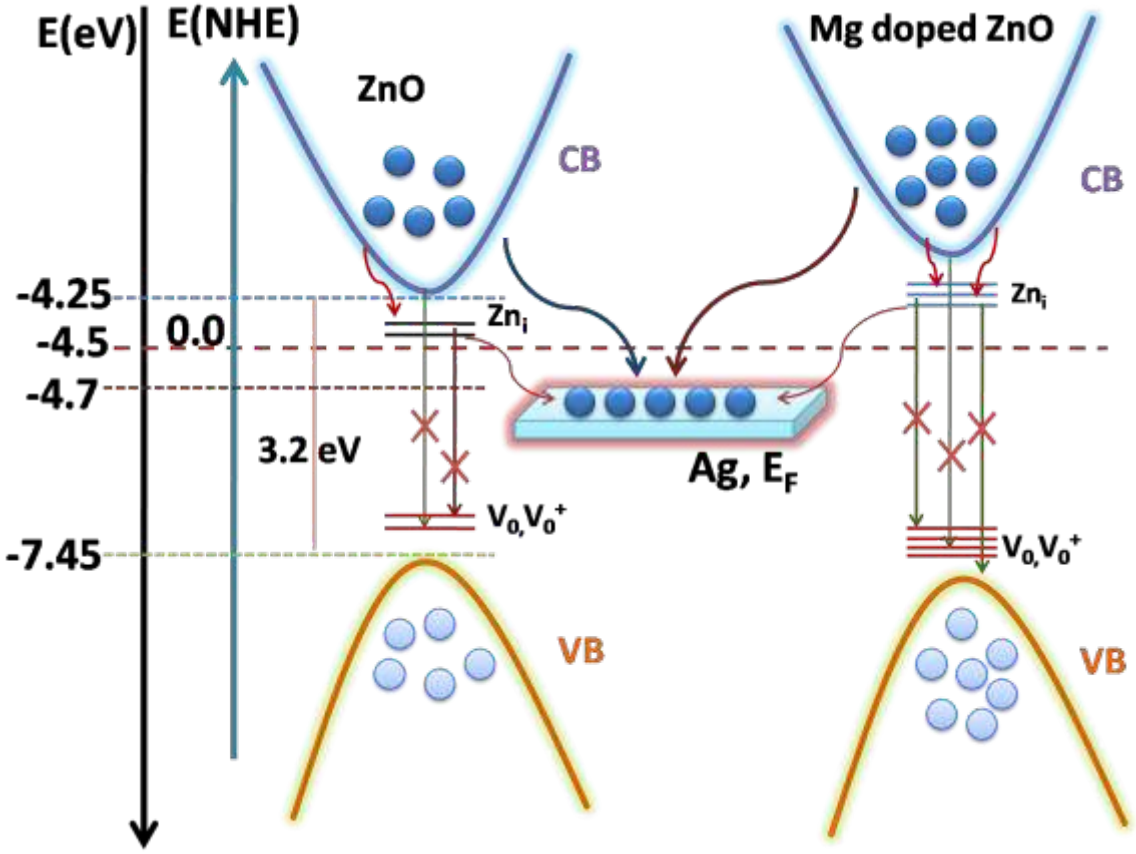

Scheme-I

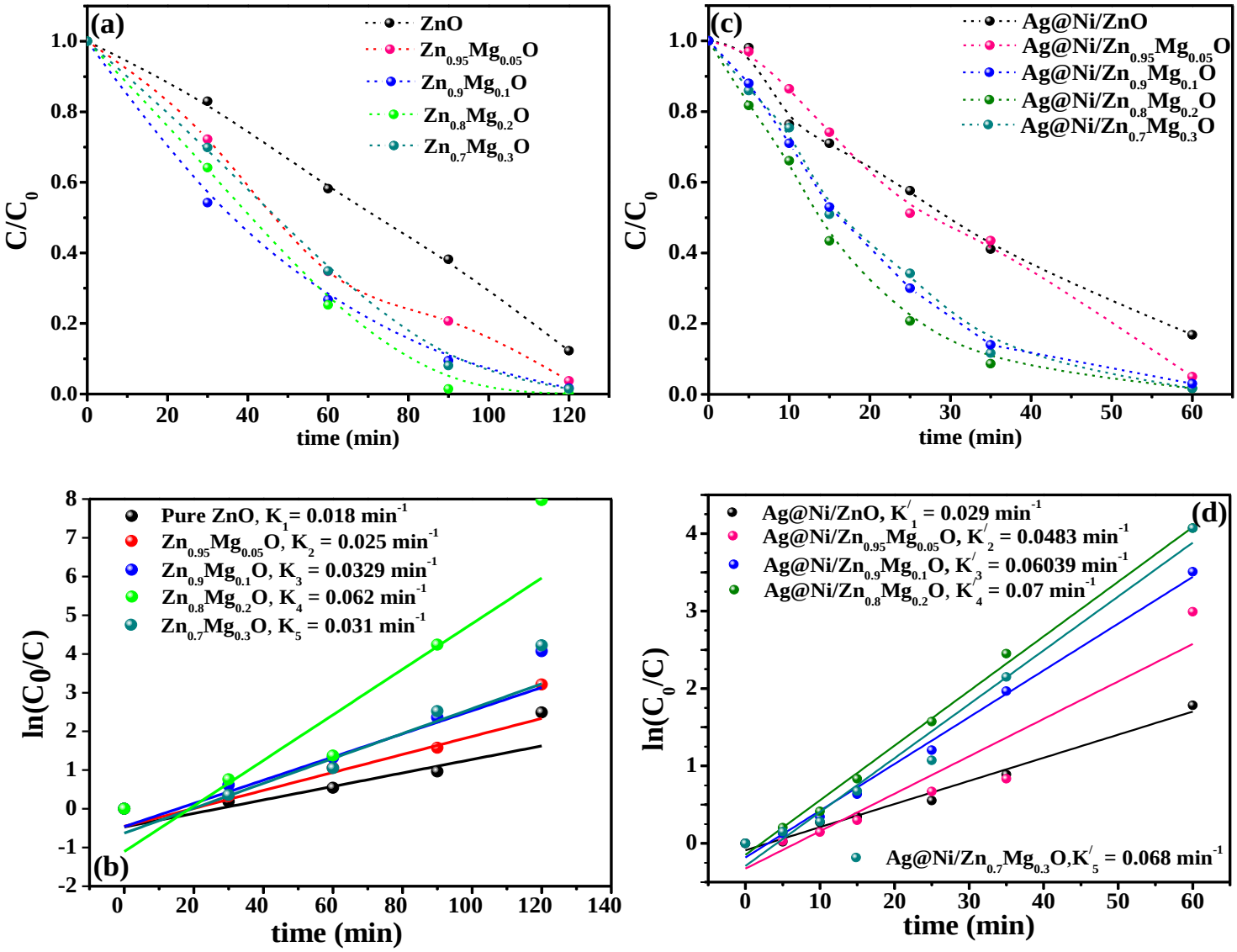

Fig. 7.

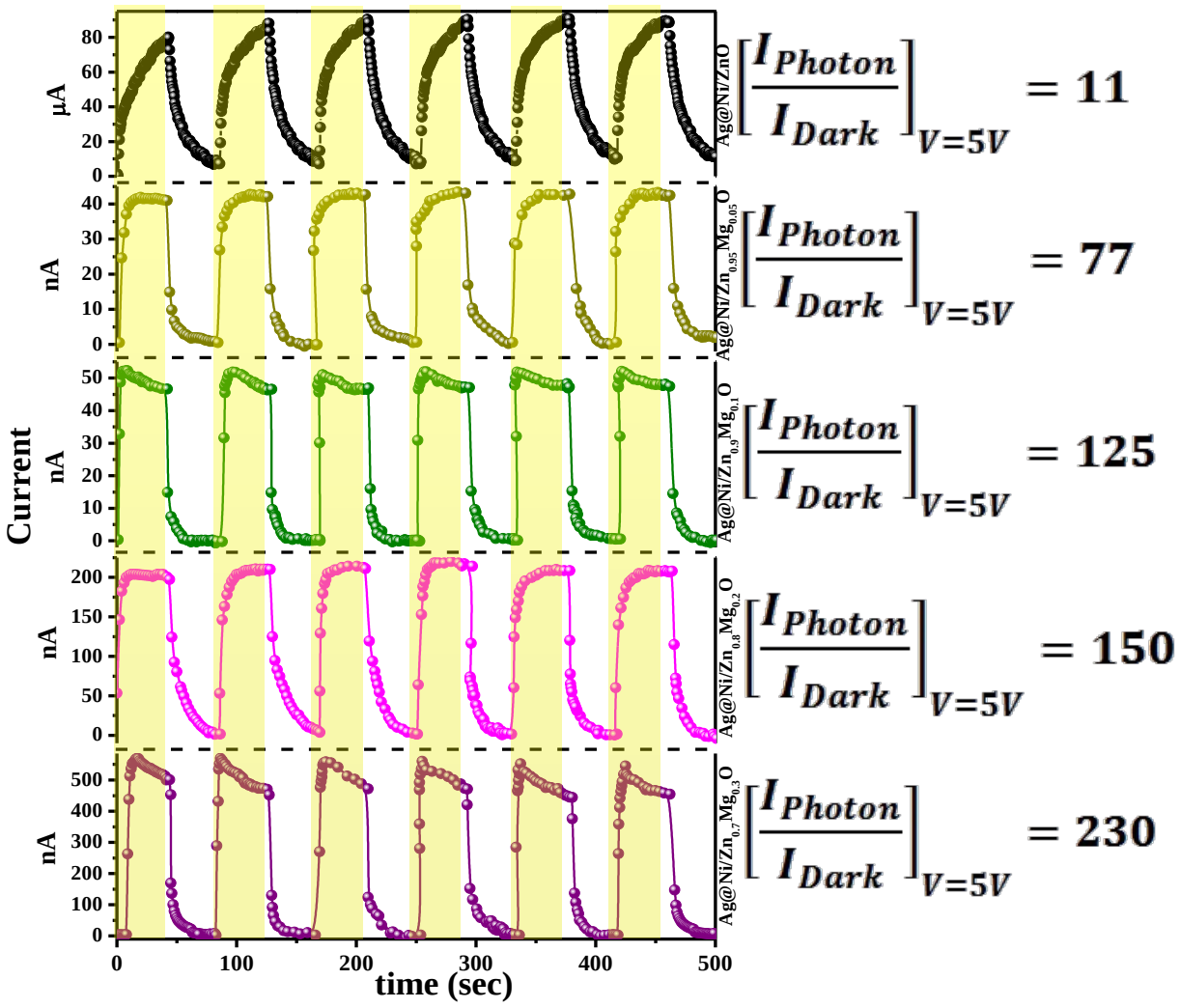

Fig. 8.

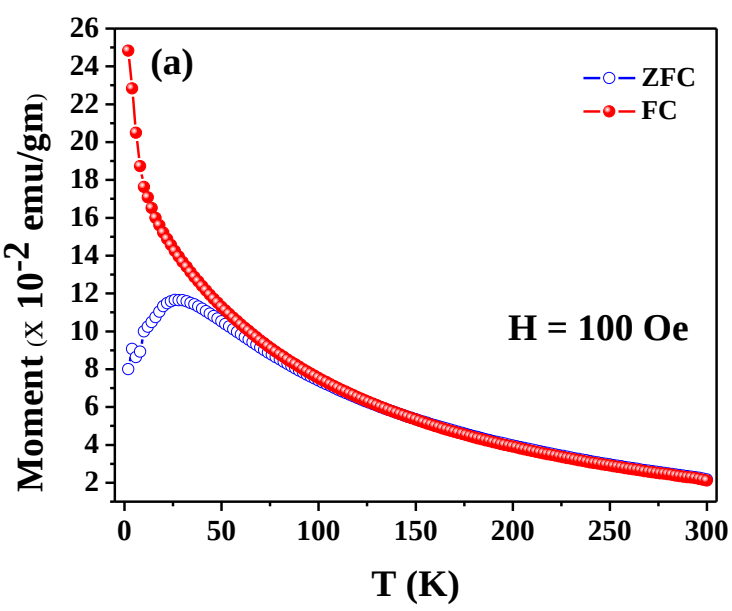

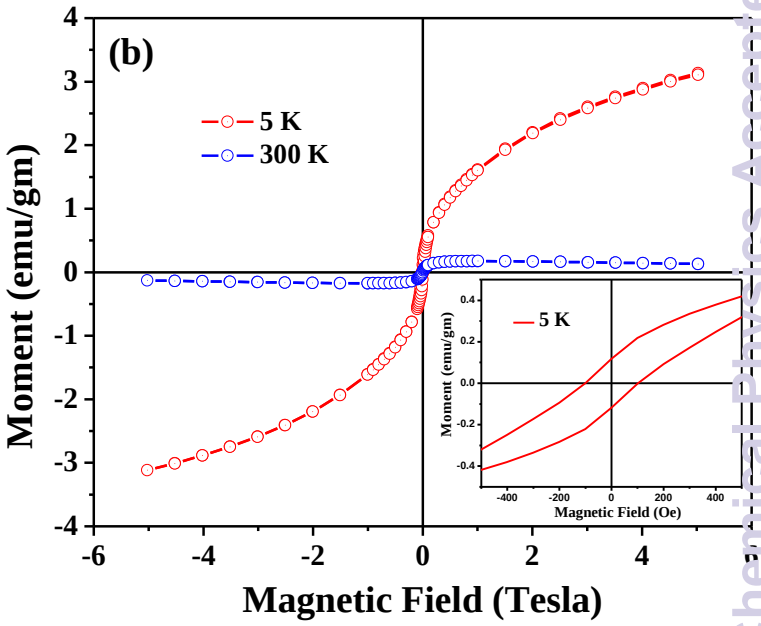

Fig. 9.